DALHOUSIE UNIVERSITY
Inspiring Minds

CALCITE FRACTURE-FILLING: A PROXY FOR GEOTHERMAL ENERGY SYSTEMS, AND IMPLICATIONS FOR THE TECTONIC HISTORY OF THE NORTHEASTERN MIDLAND VALLEY, SCOTLAND

Jacob VanderWal

SUBMITTED IN PARTIAL FULFILLMENT OF THE REQUIREMENTS FOR THE
DEGREE OF BACHELOR OF SCIENCES, HONOURS
DEPARTMENT OF EARTH SCIENCES
DALHOUSIE UNIVERSITY, HALIFAX, NOVA SCOTIA
APRIL 2018

Distribution License

DalSpace requires agreement to this non-exclusive distribution license before your item can appear on DalSpace.

NON-EXCLUSIVE DISTRIBUTION LICENSE

You (the author(s) or copyright owner) grant to Dalhousie University the non-exclusive right to reproduce and distribute your submission worldwide in any medium.

You agree that Dalhousie University may, without changing the content, reformat the submission for the purpose of preservation.

You also agree that Dalhousie University may keep more than one copy of this submission for purposes of security, back-up and preservation.

You agree that the submission is your original work, and that you have the right to grant the rights contained in this license. You also agree that your submission does not, to the best of your knowledge, infringe upon anyone's copyright.

If the submission contains material for which you do not hold copyright, you agree that you have obtained the unrestricted permission of the copyright owner to grant Dalhousie University the rights required by this license, and that such third-party owned material is clearly identified and acknowledged within the text or content of the submission.

If the submission is based upon work that has been sponsored or supported by an agency or organization other than Dalhousie University, you assert that you have fulfilled any right of review or other obligations required by such contract or agreement.

Dalhousie University will clearly identify your name(s) as the author(s) or owner(s) of the submission, and will not make any alteration to the content of the files that you have submitted.

If you have questions regarding this license please contact the repository manager at dalspace@dal.ca.

Grant the distribution license by signing and dating below.

_____ _____

Name of signatory Date

- ABSTRACT -

Geothermal energy has emerged as a reliable, cost-effective, and sustainable energy resource in areas of tectonic activity where hot sub-surface fluid circulation is common. Precipitation of carbonates within fractures that act as fluid conduits can act to modify and reduce flow, acting as a limiting factor to geothermal energy production. It is therefore important to understand the relationship between mineral precipitation, fluid source, and precipitation temperatures when assessing the economic potential of a geothermal locality. Here we present optical and cathodoluminescence (CL) petrography, $\delta^{13}C$ and $\delta^{18}O$ stable isotope data, minor and trace element analyses, U-Pb dating, and clumped isotope temperature calculations for six carbonate veins collected from a 'fossil' analogue (easily accessible) basalt-hosted (Montrose Volcanic) geothermal system in Lunan Bay Scotland, part of the Midland Valley Terrane. Calcite growth is observed as stretched and bladed crystals likely formed during active fracturing, and blocky, altered crystals indicative of post-fracture precipitation. CL signatures (suggestive of changes in minor element concentrations Fe^{2+} and Mn^{2+}) exhibit relatively constant signatures across most veins and amygdales, disconnected from fluctuations seen in Fe^{2+} and Mn^{2+} concentrations as well as $\delta^{13}C$ and $\delta^{18}O$ values. U-Pb calcite vein ages suggest Mid Devonian to Mid Carboniferous vein precipitation, while clumped isotope paleothermometry gives vein precipitation temperatures between 120 and 190 ^{o}C for vein samples, and 70 ^{o}C for amygdales. These temperatures are out of equilibrium with calcites expected to have precipitated from meteoric fluids within ambient bedrock temperatures and are therefore likely to have a magmatic-meteoric magmatic fluid-source, as is supported by back-calculated $\delta^{18}O$ calculations. Complex bedrock buffering of the fluids is also suggested, supported by the minor and isotopic variations mentioned above, as well as LREE enriched, chondrite normalized REE trends. The findings of this study have implications towards the age of Montrose Volcanic formation deposition (younger than previously suggested), and suggest that prolonged, subsurface igneous activity no longer observed within the rock record continued within the northern Midland Valley Terrane into the Carboniferous. Furthermore, the methodologies applied within this study (primarily U-Pb dating in conjunction with clumped isotope paleothermometry) show potential to accurately date and determine the temperature of calcite scaling within active geothermal systems, providing insights into the economic potential of a geothermal locality.

Keywords: calcite veining, fracture-filling, clumped isotope paleothermometry, stable isotopes, U-Pb dating, geothermal energy, Scotland, Midland Valley

- TABLE OF CONTENTS -

- LIST OF TABLES -

- LIST OF FIGURES -

- LIST OF ABBREVIATIONS -

Andesitic Basalt – and. bslt.
Calcite – ct.
Chlorite – chl.
Electron Microprobe Micro-Analyzer – EMPA
    Heavy - HREE
    Light – LREE
    Medium – MREE
Laser Ablation Inductively Coupled Plasma Mass Spectrometry – LA-ICPMS
Midland Valley Terrane - MVT
Montrose Volcanic Formation – MVF
Multiply substituted 'clumped' isotope paleothermometry - Δ_{47}
Old Red Sandstone – ORS
    Lower – LORS
    Upper – UORS
Parts per billion - ppb
Parts per million - ppm
Parts per thousand – ‰
Plagioclase – plag.
Quartz – qtz.
Rare Earth Elements – REE
Sandstone – ss.
Standard deviation - Std. Dev., σ
Standard error – Std. Er.
Vienna Pee Dee Belemnite - VPDB
Vienna Standard Mean Ocean Water - VSMOW
Weight percent – wt.%

- ACKNOWLEDGEMENTS -

I would like to thank my fellow classmates, the Dawson Geology Club, and everyone else within Dalhousie's Earth Science Department and the University of Glasgow's Department of Geographical and Earth Sciences for their support and aid over the past four years. I am also grateful to Dr. John Faithfull, John Gilleece, Dr. Nick Roberts, Warren Joyce, Dan MacDonald and Dr. James Brenan for help with various analyses, and to Dr. Ian Winkelstern for stepping in to help me out in a bind! Thanks to the Dalhousie SELF Fund and the SEG Canada Foundation for help financing this research, and to Dr. Owen Sherwood for his help with those funding initiatives. Thanks also to Dr. Djordje Grujic and the rest of the honours class for continual encouragement throughout the year. Finally, I would like to thank my supervisor, Dr. John MacDonald, for putting up with me (his first and likely last long-distance honours student!), but mostly for being a great supervisor.

- Chapter 1: INTRODUCTION -

1.1 Background

1.1.1 Introduction to Geothermal Energy & Fluid Flow Issues

There has been increased interest in finding and exploiting renewable, low impact, energy sources given the estimated 3 Ga rise in the human population by 2050, and the resulting energy requirements this growing population will require (DESA 2017, Glassley 2015). Geothermal energy has emerged as a reliable, cost-effective, and sustainable energy resource to meet these increased energy needs and has the potential to play an important role in the transition away from fossil fuel-sourced energy. In short, geothermal energy uses the heat energy provided by the cooling of the earth and the decay of long-lived radioactive isotopes (U, Th, and K) contained within the upper 5-10 km of the continental crust to provide energy for human consumption (Glassley 2015). Traditional exploitation of geothermal energy has been largely focused on areas of tectonic activity (western US, Iceland, the Philippines, and New Zealand), where hot (160-250 ^{o}C) naturally occurring waters are easily circulated through the crust via a fractured (or porous) bedrock medium.

It is therefore important that the permeability (and to a lesser extent, porosity) of the reservoir host-rock is maintained in order to allow for continuous fluid circulation. However, high temperature geothermal fluids often act as strong solvents, interacting with the host bedrock and carrying dissolved volatile elements and species (e.g. H_2S, HCO_3^-, SO_4^{2-}) within solution (Glassley 2015). Many of these solutions are phase dependent and will precipitate back out of solution within the fluid conduits as the geothermal fluid cools, resulting in reduced bedrock permeability and restricted fluid flow (McNamara et al. 2016).

One of the most common precipitates is calcite, $CaCO_3$, which is highly dependent upon the movement of CO_2 within the reservoir (adapted from Simmons & Christenson 1993) and experiences inverse solubility with higher temperatures McNamara et al. 2016). Calcite commonly precipitates via the following equation:

$$2HCO_3^- + Ca^{2+}{}_{(sol)} = CaCO_{3(s)} + H_2CO_{3(l)} = CaCO_{3(s)} + H_2O_{(l)} + CO_{2(g)} \quad \textbf{Equation 1}$$

The precipitation of calcite in geothermal systems is less of an issue where tectonic activity maintains fractured fluid pathways but can raise costs within enhanced

geothermal systems where active hydraulic fracturing of the bedrock is required in order to create said pathways. Much of Earth's population growth is expected to occur in areas that lack the tectonic activity required to maintain surface-subsurface fluid circulation (e.g. the west coast of Africa, mainland India and China). Understanding the relationship between mineral precipitation, fluid source and precipitation temperature when assessing the economic potential of a geothermal locale is therefore crucial.

1.1.2. Overview

Calcite precipitation has been the focus of many studies based on fluid source and flow in active and fossil geothermal systems (e.g. Maskenskaya et al. 2015; McNamara et al. 2016; Morad et al. 2010; Wogelius et al. 1997). Geochemical analyses focused on minor elements and REE have been employed on bulk-vein samples to fingerprint the source of the mineralizing fluid, the degree of fluid-bedrock interaction, and changes in fluid chemistry. (Barker & Cox 2011; Denniston 1997; Morad et al. 2010), while finer scale investigations have focused on temporal changes and growth mechanisms within individual veins (Barker et al. 2006; Bons et al. 2012; Hilgers et al. 2000, 2004; McNamara et al. 2016; Ramsay 1980). Many of these studies have also utilized stable isotopes of oxygen and carbon to assess the source of geothermal fluids (Barker et. al 2006; Blyth et al. 2004; Hilgers & Sindern 2005; Lee et al. 1997; Maskenskaya et al. 2015; Morad et al. 2010; Sandström & Tullborg 2009; Sumner et al. 2015; Wogelius et al. 1997). However, determinations of absolute age and temperature of formation have been more challenging; the former relies dating host rock materials or crosscutting species (Maskenskaya et al. 2015), while the the latter utilizes on fluid inclusion studies and $\delta^{18}O$ geothermometry subject to fluid resetting and assumptions on the initial fluid composition not always known (MacDonald et al. 2017; Maskenskaya et al. 2015; Sturrock et al. 2017).Two new methods have been developed to address these shortfalls: calcite U-Pb geochronology (Coogan et al. 2016; Roberts et al. 2016; Roberts & Walker 2016), and clumped isotope paleothermometry (Bergman et al. 2013; Coggon & Teagle 2011; Lu et al. 2017; MacDonald et al. 2017; Sumner et al. 2015).

1.1.2.2 Mineral Growth & Fracture Sealing Mechanisms

Studies on fracture filling calcites have noted different growth mechanisms; syntaxial or stretching growth from vein edge to centre during fracture opening

(McNamara et al. 2016), and antitaxial growth from the vein centre (Figure 1) (Barker et al. 2006; Bons et al. 2012). However, there are also difficulties in discerning mineral sealing processes from microstructural data due to a wide range of factors, including rates of fluid flow (Hilgers et al. 2004), unknown deformation rates (McNamara et al. 2016), temperature variations, and discrete growth phases (Barker et al. 2006; Hilgers & Sindern 2005; Sumner et al. 2015). All of these factors need to be taken into consideration when analyzing the degree of bedrock buffering or variations in isotopic conditions.

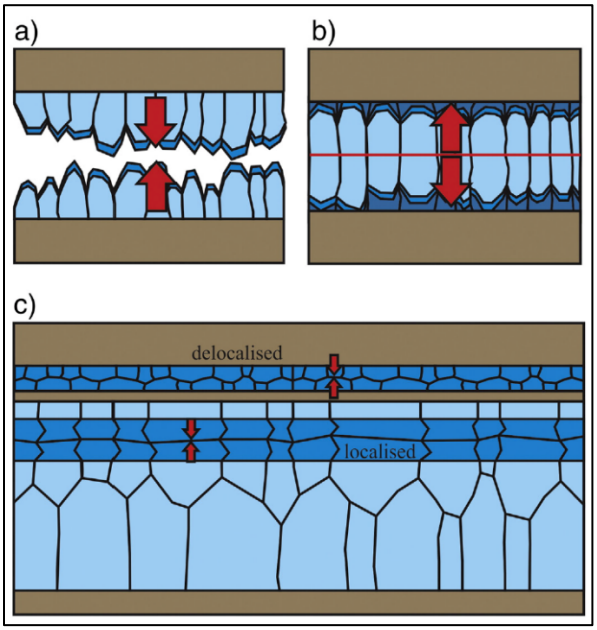

Figure 1. Various forms of mineral growth within fractures. a) syntaxial sealing, where vein growth becomes elongate in the direction of growth during crack-sealing deformation events b) antitaxial sealing, where crystals grow from a nucleating medium outwards towards the bedrock, and c) stretching vein showing both delocalised vein growth (fracture propagation from wall rock with new material) and localised vein growth (fracture propagation within an already active fracture zone). From McNamara et al. 2016.

1.1.2.3 Geochemical Analyses & Fluid-Bedrock Interactions

The concentration and distribution of minor and trace elements has been used to identify the fluid sources from which calcite precipitates. Cooler meteoric waters percolating down through open fractures are less likely to react with the country rock than upward-flowing hot magmatic/hydrothermal fluids, which are therefore more likely to precipitate calcite with higher concentrations of minor elements (Morad et al. 2010; Wogelius et al. 1997). Large variations in REE analyses are likely the result of continuous element depletion (Barker et al. 2006), mixing source fluids (Maskenskaya et al. 2013; Wogelius et al. 1997) or variations in calcite crystallization condition (Denniston et al. 1997). However, studies commonly note the reliance on mineralization conditions not encompassed within the scope of analyses, as well as a lack of a fluid

proxy known to have precipitated directly from the host rock. These pose challenges to conclusively determine the source fluid origin or bedrock buffering within calcite precipitation studies.

1.1.2.4 C & O Stable Isotopes

Stable isotopes are isotopes of the same element that do not experience radioactive decay and are therefore considered useful as they often experience fractionation via a number of natural processes. This fractionation is due to the difference in atomic mass of the stable isotopes of a given elements, which are then preferentially included in various mineral assemblages or natural processes as a result. Relevant to this study are oxygen and carbon, with the former primarily fractionating between ^{18}O (mass 17.999u, - 0.1995% natural abundance) and ^{16}O (mass 15.995u - 99.763% natural abundance) and the latter between ^{13}C (mass 13.003u – 1.11% natural abundance) and ^{12}C (mass 12.001u - 98.89% natural abundance) (Rollinson 1993). These fractionation processes are dependent upon temperature, fluid pH, and mineral species (amongst other factors), but can often be used to compare source rock and fluid-rock interactions (Rollinson 1993). Absolute isotopic values are inconvenient for isotopic comparison, so δ notation (in parts per thousand, ‰) is used to measure the ratio of heavy versus light isotopes, as defined by the following equations:

$$\delta^{18}O = \left(\frac{\left(\frac{^{18}O}{^{16}O}\right)_{sample}}{\left(\frac{^{18}O}{^{16}O}\right)_{standard}} - 1 \right) \times 1000\,{}^{o}/_{oo} \qquad \textbf{Equation 2}$$

$$\delta^{13}C = \left(\frac{\left(\frac{^{13}C}{^{12}C}\right)_{sample}}{\left(\frac{^{13}C}{^{12}C}\right)_{standard}} - 1 \right) \times 1000\,{}^{o}/_{oo} \qquad \textbf{Equation 3}$$

Both values are measured against a Pee Dee Belemnite (VPDB) standard (NBS-19), while $\delta^{18}O$ can also be measured against versus the Standard Mean Ocean Water (VSMOW) scale as follows:

$$\delta^{18}O_{modern\ seawater} = 0‰_{VSMOW}\ or\ -29.98‰_{VPDB} \qquad \textbf{Equation 4}$$

$$\delta^{13}C_{marine\ carbonate} = 0‰_{VPDB} \qquad \textbf{Equation 5}$$

where conversion between VSMOW and VPDB for $\delta^{18}O$ values is defined as (Rollinson, 1993):

$$\delta^{18}O_{VSMOW} = 1.03091\ \delta^{18}O_{VPDB} + 30.01 \quad \textbf{Equation 6}$$

$$\delta^{18}O_{VPDB} = 0.97002\ \delta^{18}O_{VSMOW} - 29.98 \quad \textbf{Equation 7}$$

Many studies of this nature use these $\delta^{13}C$ and $\delta^{18}O$ analyses to give an indication of fluid source and bedrock buffering (changing of the fluid signature due to host rock-fluid interaction). Small variations (<3‰) of $\delta^{13}C$ and $\delta^{18}O$ within individual veins have been suggested to be the result of bedrock buffering (Hilgers & Sindern 2005) or stable temperature and chemistry (Barker et. al 2006; Lee et al. 1997). Large variations (>6‰) may indicate various degree of fluid-host rock interaction or mixing of distinct fluid types (Wogelius et al. 1997; Maskenskaya et al. 2015). Furthermore, stable isotopes have been useful in constraining meteoric versus hydrothermal fluid sources (although temperature dependence often makes this interpretation difficult) (Maskenskaya et al. 2015; Rollinson et al. 1993).

1.1.2.5 Absolute Age Determinations

While successful in relatively young geothermal systems (Lu et al. 2017), absolute age determination of calcite fracture filling processes has historically been a challenge in fossil geothermal systems, with dates being inferred primarily from the dating of the host rock or minerals trapped during vein growth (e.g. zircons), or bulk dissolution of U-rich calcite veins material for U-Pb dating (Roberts & Walker, 2016). The first method is often only able to provide older, largely inaccurate vein precipitation given a lack of other dating techniques, while the second method is often hindered by the high Pb concentrations found within many hydrothermal systems (Roberts & Walker 2016). However, targeted analyses using newer, more accurate (smaller spot size) LA-ICPMS systems have proven useful in targeting areas of high U-low Pb, allowing for a large spread of U-Pb ratios to be obtained directly from in-situ calcite samples without having to deal with the uncertainties derived from the high common lead concentrations. (Coogan et al. 2016; Roberts & Walker 2016).

1.1.2.6 Clumped Isotope (Δ_{47}) Paleothermometry

Previous determinations of calcite precipitation temperature have been largely focused on the identification and analysis of fluid inclusions trapped within the carbonate mineral lattice (MacDonald et al. 2017; Maskenskaya et al. 2015; Sturrock et al. 2017), or the use of $\delta^{18}O$ paleothermometry where the isotopic composition of the

source fluid is known (Denniston et al. 1997; Morad et al. 2010). The first is useful, as it is able to infer burial temperature through the measurement of homogenization temperature: the point where the vapour bubble disappears, and a single-phase fluid remains (MacDonald et al. 2017). However, the former is often limited by the lack of two-phase fluid inclusions or, within fine grained rocks, the lack of any fluid inclusions at all. Furthermore, two phase inclusions can also be reset at higher temperatures, limiting the ability to accurately determine initial precipitation temperature within samples derived from depth (MacDonald et al. 2017). The $\delta^{18}O$ paleothermometer is based on the relationship between mineral $\delta^{18}O$ and that of the precipitating fluid. However, the latter is often unknown, and deviations only 1‰ off may lead to temperature estimates 10 ºC away from actual mineral precipitation temperature (MacDonald et al. 2017).

Another relatively new technique has been developed to determine carbonate precipitation temperature independent of fluid inclusions or source fluid chemistry: clumped isotope (Δ_{47}) paleothermometry. Δ_{47} focuses on how multiply substituted isotopologues (molecules of similar chemical but different isotopic composition, containing two or more heavy isotopes) of CO_2 are arranged within the carbonate crystal lattice (Table 1) (Eiler 2007). These multiply substituted isotopologues are more thermodynamically stable than singly substituted isotopologues, with lower bond vibrations and therefore lower energy states (Eiler, 2007). These isotopologues are temperature dependent and are considered to be at stochastic distribution at thermodynamic equilibrium (1000 ºC), where preferential clumping is overtaken by the entropy of the system. At this temperature, carbonate minerals are expected to contain abundances of $^{13}C^{18}O^{16}O_2^{-2}$ ionic groups defined by (Schauble et al. 2006):

$$Ca^{12}C^{18}O^{16}O_2 + Ca^{13}C^{16}O_3 = Ca^{13}C^{18}O^{16}O_2 + Ca^{12}C^{16}O_3 \qquad \textbf{Equation 8}$$

Clumped isotopes are measured as Δ_I, where Δ_I is the measure of excess or deficit isotopologue *i* relative to the amount expected within a conformable stochastic distribution (Eiler 2007).The most common measure of Δ_I is the Δ_{47} value for CO_2, which reflects variations in the abundance of $^{13}C^{18}O^{16}O$ (the most common multiply substituted isotopologue of CO_2) (Table 1) (Eiler 2007). Δ_{47} is calculated as follows:

$$\Delta_{47} = \left[\left(\frac{R^{47}}{R^{47*}} - 1\right) - \left(\frac{R^{46}}{R^{46*}} - 1\right) - \left(\frac{R^{45}}{R^{45*}} - 1\right)\right] \times 1000 \qquad \textbf{Equation 9}$$

where:

R^{47} = abundance ratio mass (47/44) for standard CO_2 **Equation 11**

R^{46} = abundance ratio mass (46/44) for standard CO_2 **Equation 12**

R^{45} = abundance ratio mass (45/44) for standard CO_2 **Equation 13**

$$R^{45*} = 2R^{13}R^{18} + 2R^{17}R^{18} + R^{13}(R^{17})^2$$ **Equation 14**

$$R^{46*} = 2R^{18} + 2R^{13}R^{17} + (R^{17})^2$$ **Equation 15**

$$R^{47*} = R^{13} + 2R^{17}$$ **Equation 16**

Variables R^{13}, R^{17} and R^{18} are the abundance ratios of $^{13}C/^{12}C$, $^{17}O/^{16}O$ and $^{18}O/^{16}O$ (respectively) for the sample at stochastic distribution. R^{13} and R^{18} are derived from the measured $\delta\ ^{13}C_{VPDB}$ and $\delta\ ^{18}O_{VSMOW}$ values of the sample, and R^{17} is calculated from R^{18} (Eiler 2007). Temperature (K) can then be constrained via the following equation (Dennis 2011).

$$\Delta_{47} = [(0.0362 \pm 0.0018)*10^6]/ T^2 - (0.2920 \pm 0.0194)$$ **Equation 17**

Table 1. Isotopologues of CO_2, with molecular mass and relative abundance (after Eiler, 2007).

Mass (CO_2^*)	Isotopologue	Relative Abundance
44	$^{12}C^{16}O_2$	98.40 %
45	$^{13}C^{16}O_2$	1.11 %
45	$^{12}C^{17}O^{16}O$	748 ppm
46	$^{12}C^{18}O^{16}O$	0.40 %
46	**$^{13}C^{17}O^{16}O$**	**8.4 ppm**
46	**$^{12}C^{17}O_2$**	**0.141 ppm**
47*	**$^{13}C^{18}O^{16}O$**	**44.4 ppm**
47	**$^{12}C^{17}O^{18}O$**	**1.50 ppm**
47	**$^{13}C^{17}O_2$**	**1.60 ppb**
48	**$^{12}C^{18}O_2$**	**3.96 ppm**
48	**$^{13}C^{17}O^{18}O$**	**16.8 ppb**
49	**$^{13}C^{18}O_2$**	**44.5 ppb**

Note: bolded are multiply substituted isotopologues. * is the primary isotopologue used for clumped isotope analysis.

The main advantage of Δ_{47} is that temperature of formation can be determined independent of known source fluid $\delta\ ^{18}O$, required in standard $\delta\ ^{18}O$ geothermometry, or the presence of fluid inclusions. However, Δ_{47} becomes unreliable at temperatures above 225 ^oC, where temperature is significantly hot enough for bond reordering. Specifically, this bond reordering involves the breakage of C-O bonds within the originally precipitated mineral lattice, and reforming of these bonds with neighbouring, allochthonous C and O and other elemental species housed within the mineral lattice

via solid-state diffusion (Henkes et al. 2014). Given the extremely small concentrations of $^{13}C^{18}O^{16}O$ that Δ_{47} analyses are based upon, even miniscule amounts of bond-reordering can lead to drastically different temperature derivations, even within closed systems and without changes in texture, $\delta^{18}O$, or $\delta^{13}C$ calculations (Henkes et al. 2014). Therefore, bond-reordering is a significant factor, especially within prolonged periods of heat, that must be taken into consideration when determining the age of hydrothermal calcites that may have been reheated via subsequent tectonic activity (Eiler 2007; MacDonald et al. 2017). Regardless recent studies have found Δ_{47} recording original precipitation temperatures between 15 °C (Eiler 2011) and 350 °C, (Bonifacie et al. 2017; Lloyd et al. 2017; Ryb et al. 2017), showing the wide range of studies Δ_{47} can be applied to. Some of these studies include paleoclimate reconstruction (Coggon & Teagle 2011), paleo-fluid migration and fracture connectivity along fault zones (Bergman et al. 2013; Sumner et al. 2015), and discrimination between multiple source reservoirs in an active geothermal locality (Lu et al. 2017).

Assuming that Δ_{47} temperature calculations are representative of initial precipitation fluid temperature, Δ_{47} analyses can then be used to back-calculate the initial $\delta^{18}O$ using the following equation (after Kim & O'Neil 1997)

$$1000\ln\alpha_{calcite\text{-}water} = [(18.03 \times 10^6) \times T^{-1}] - 32.42 \qquad \textbf{Equation 18}$$

where T represents the precipitation temperature (K) and $\alpha_{calcite\text{-}water}$ is the fractionation factor between calcite and water ($‰_{VSMOW}$).

1.2 Purpose & Objectives

The purpose of this study is to further the understanding of factors affecting calcite fracture filling, and to place constraints on the effects of fluid-bedrock interaction, fluid source, deposition temperature and age of deposition in geothermal systems. This will be conducted using a case study fossil geothermal system located in Lunan Bay, Scotland, given the ease of sample access and spatial coverage not available through traditional well-based studies.

Three objectives will be addressed in this research:

(1) Assessing the degree of bedrock-fluid interaction and potential fluid source, based upon optical and CL petrography, minor element and REE geochemical

analyses, and in-situ stable isotope measurements of veins and bedrock-derived amygdales.

(2) Determining a potential age of vein formation using U-Pb calcite geochronology and relating these ages to published burial histories of the region.

(3) Gauging calcite precipitation temperature using Δ_{47} analyses and applying these to place constraints on the findings of objectives (1) and (2).

1.3 Thesis Outline

This thesis will employ a wide range of techniques in order to achieve the objectives listed in Section 1.2. Textural analyses and CL microscopy will be employed in an attempt to outline various forms of mineral growth, fracture sealing mechanisms, and any qualitative changes in fluid chemistry (Section 5.1). Next, the temperature and timing of calcite precipitation will be interpreted using clumped isotope (Δ_{47}) paleothermometry and LA-ICPMS U-Pb dating – the first time these two techniques have been employed together in a study of this type (Section 5.2). Finally, to determine the degree of fluid-bedrock interaction as well as a potential fluid source, Electron Microprobe Micro-Analyzer (EMPA) and LA-ICPMS analyses of minor elements Fe^{2+} and Mn^{2+}, stable isotope analyses of C and O isotopes, and LA-ICPMS REE analyses will be used in conjunction with the (Δ_{47}) temperature determinations (Section 5.3). In order to address a common pitfall – the lack of a bedrock chemical proxy for comparison with precipitating fluids - noted in previous studies (Barker et. al 2006; Hilgers & Sindern 2005; Lee et al. 1997; Maskenskaya et al. 2015; Wogelius et al. 1997), this study will employ a new analytical technique. By analyzing a series of bedrock amygdales using the same techniques employed on the vein samples, minor elements, REE and isotopic compositions can be compared to fluids assumed to have been precipitated from a bedrock source, and the degree of bedrock-fluid buffering can then be determined (Section 5.3). The results of this study will then be applied to known burial models for the region in order to place constraints on MVF formation and provide interpretations for the tectonic history of the region (Section 5.4). Finally, the results and methodologies employed within this study will be discussed with regards to how they may be used to inform current research regarding geothermal energy (Section 5.5).

- Chapter 2: GEOLOGICAL SETTING -

2.1 Study Area

The area of interest for this study is located at the north end of Lunan Bay, approximately 5km due south of Montrose, along the east coast of Scotland (Figure 2). Preliminary reconnaissance by Dr. John Faithfull (Hunterian Museum, University of Glasgow) noted significant carbonate veining within easily accessible volcanic host rocks.

2.2 Tectonic, Sedimentary & Volcanic Setting

The study area is located within the northern part of the Midland Valley Terrane (MVT). The MVT was first recognized as a rift valley (George 1960; Kennedy 1958) but is now widely recognized as a former volcanic arc that accreted to Laurentia (more specifically, the Dalradian Terrane) during the Ordovician (~470-460 Ma) (Armstrong & Owen 2001; Bluck et al. 1992; Dalmeyer et al. 2001; Stone 2014). With a reversal in subduction during the late Silurian (~420 Ma) the Baltica and Avalonia cratons accreted into the MVT, resulting in the closure of the Iapetus Ocean basin (Hole et al. 2013). Following this closure, up to 9km of Lower Old Red Sandstone sediments (primarily conglomerates and sandstones sourced from Laurentia) were deposited onto the MVT and into the Iapetus Ocean basin (Marshall et al. 1994). Sporadic volcanic activity within the region also continued during this time, resulting in the interfingered sedimentary-volcanic packages now seen today (more in Section 1.3.3) (Hole et al. 2013; Marshall et al. 1994). After a period of non-deposition during the Middle Devonian, Upper Old Red Sandstone sandstones and conglomerates were deposited onto the Lower Old Red Sandstone packages during a period of alluvial/ fluvial controlled sediment transport (Bluck, 2000; Browne et al 2002; Rawley, 2015) (Figure 2).

The study area itself is composed primarily of the ~560 m thick Montrose Volcanic Formation (MVF), a group of mingled pahoe-hoe lavas, basaltic andesites, and volcanic-derived sediments deposited as part of the ~2000 m thick, sandstone dominated Arbuthnott-Garvock Group (Figure 2) (Armstrong & Paterson 1970; Browne et al. 2002; Bluck 2000; Hole et al. 2013). These lavas are likely sourced from the northern flank of the Montrose Volcanic Centre, a north-east to south-west trending chain of volcanoes active for ~15 Ma. The MVF lavas are suggested to be coeval with

the Rhynie lavas to the north, with a U-Pb andesite age of 411.5 ± 1.3 Ma (Parry et al. 2011). This places the MVF within the late Lochkovian – early Pragian and at the boundary of the Arbuthnott and Garvock units (Hole et al. 2013; Rawley 2015).

2.3 MVF Host Rock Petrography

The MVF lavas are basaltic to basaltic andesite (5.2-8.6 wt.% MgO, 52.6-57.6 wt.% SiO_2) in composition, and samples from St. Cyrus region have been described as olivine-plagioclase phyric, with olivine commonly pseudomorphed to iddingsite (Thirwall 1981; 1982; 1983). Sub-euhedral, tabular, microphenocrystic plagioclase feldspar (labradorite to low Ab andesine, An_{41-55}) make up much of the matrix, along with abundant interstitial devitrified glass (Thirwall 1982). Clinopyroxene is also present within some of the pahoehoe lava flows, predominantly in the form of augite (Hole et al. 2013). The lavas are also interbedded with locally sourced ephemeral playa-lake sediments, sandstones, and conglomerates, as well as air fall eruptions, creating complex sediment-lava interactions and abundant peperite formation (Hole et al. 2013; Trewin & Thirlwall 2002; Woodcock and Strachan 2008). Within these mixing regions, secondary orthoclase is also present, as is sub-parallel flow alignment of feldspar laths and microphenocrysts (Thirwall 1982; 1983).

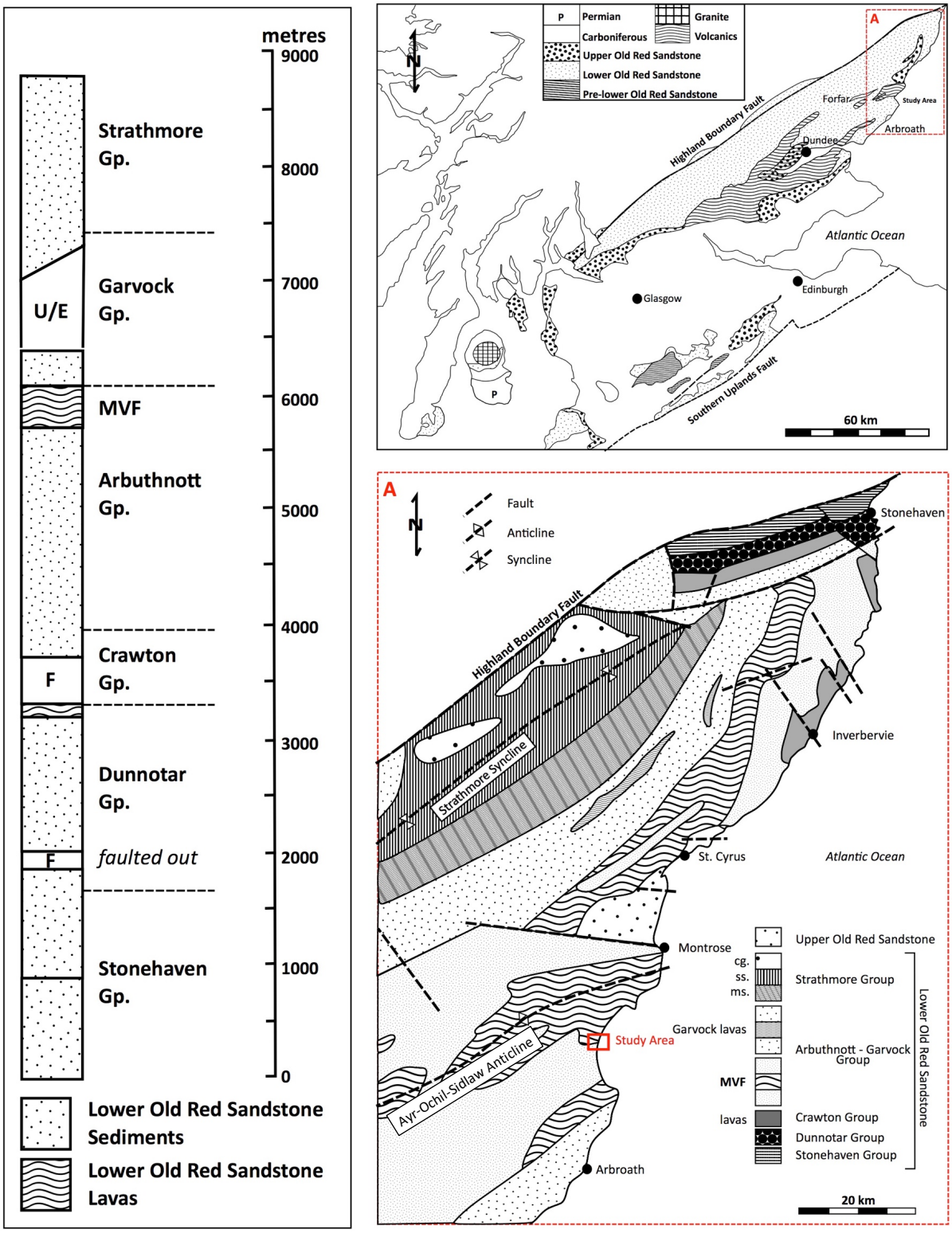

Figure 2. Top right: simplified regional geological map of the Midland Valley, Scotland with inlay of study area (A) and bounding faults. Bottom right: geological map of the east coast of Scotland from Stonehaven to Arbroath, showing study area in red. Left: lithostratigraphic relationships for the area covered by inset (A). Study area in Red. After Hole et al. 2013 and Marshall et al. 1994.

2.4 Regional Burial History

Based on vitrinite reflectivity values for the Forfar region based on remnant plant matter, and assuming stratigraphic continuation with other parts of the MVT and a geothermal gradient of 30 ^{o}C/km, Marshall et al. (1994) established a potential burial model for the region of interest (Figure 3). The model suggests rapid burial of the MVF to ~2.6 km from deposition in the early Devonian until the mid-Devonian, followed by uplift to ~1.3 km in the late Devonian- early Carboniferous, both suggested to be effects of the larger Acadian Orogeny (Browne et al. 2002). Maximum burial of the MVF at ~3.75 km then occurred at the Carboniferous-Permian boundary. A final cycle of uplift (Permian-Triassic boundary; ~2.1 km), burial (Cretaceous-Paleogene boundary; ~3.0 km) and an uplift has brought the MVF to the surface by the present day. Given that Forfar is only 10 km to the west of Lunan Bay, these data are likely relatively accurate estimates of burial/ uplift for the area of interest within this study.

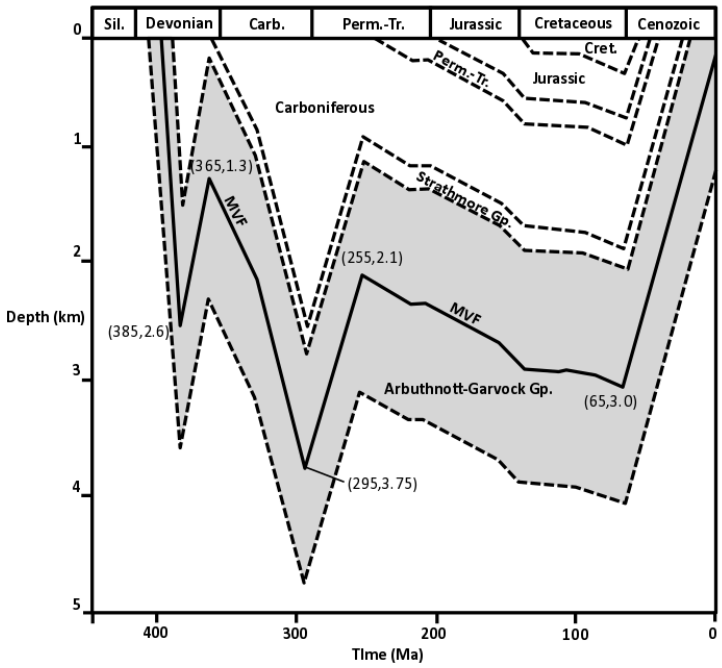

Figure 3. Burial history for the lower ORS and Arbuthnott-Garvock group (gray) from the Forfar area with the MVF and corresponding values (age, depth) included. Strata based upon back stripping from the Lower ORS sequence together with now eroded stratigraphy based upon relationships seen in other areas of the MVT and Northern Ireland. After Marshall et al. 1994.

- Chapter 3: METHODS -

3.1 Field Methods

Un-oriented samples were collected in the field on February 15th, 2017 and May 12th, 2017. Effort was made to collect vein samples with both bedrock interfaces intact. However, due to the brittle nature of some samples, this was difficult at times (samples JV17-1a and JV17-9 are examples of this).

3.2 Laboratory Methods

3.2.1 Sample Preparation

Samples were selected based upon prominent veining within the host rock; all attempts were made to include both vein and host material, although some larger veins have limited host rock presence due to the brittle nature of the samples. Samples were made into polished thin sections, with corresponding rock chips preserved for further analysis.

3.2.2 Optical Petrography

Optical petrography was undertaken using the Lumin HC4-LM hot-cathode CL microscope (Section 2.2.3) in order to distinguish between carbonate and non-carbonate/ host rock species within each slide. Photo collages were stitched together and orthorectified to thin section scans using Photoshop CS5 and Inkscape software.

3.2.3 Cathodoluminescence (CL) Petrography

Calcite CL is highly dependent upon composition, lattice structure, and impurities/ alteration within a given mineral (Machel 1985; SERC 2016). However, the most prominent variations in CL signature are due to minor element concentrations, with Fe^{2+} ions acting as the main quenchers (luminescing an orange-red colour) and Mn^{2+} (and to a lesser extent, trivalent REE) ions acting as the main activators (LeRouge et al. 2010). Variations in CL signature are often inferred as changes in elemental concentrations or chemical zonation within carbonates (Blyth et al. 2004; McNamara et al. 2016).

CL petrography was undertaken using the Lumin HC4-LM hot-cathode CL microscope with a Varian turbomolecular vacuum pump at Saint Marys University. Polished slides were carbon coated using a Leica EM CED-030 carbon coater to

prevent slide damage due to concentrated electron build-up. Samples were placed face down within the vacuum chamber of the microscope. Plane-polarized and CL imagery was taken using the incorporated Olympus BXFM focusing unit and Kappa DX40C peltier cooled camera, controlled by the DX40C-285FW software package. The samples were analyzed under a vacuum, with an accelerating voltage of ~6 KV, a beam current of 0.25 mA, and a 1 s camera exposure time. Photo collages were then stitched together using methods similar to those described in Section 2.2.2.

3.2.4 Electron Microprobe Analysis

Electron Microprobe Micro-Analyzers (EMPA) accelerate a beam of electrons across a heated tungsten metal filament and through a series of lenses that condense and focus the beam. When the high energy electrons hit the sample, they excite the atoms of the sample material, generating X-rays unique to different elements. These X-rays are collected, counted, and measured against known standards in order to determine the chemical composition of the spot (USGS, 2015).

EMPA analyses were undertaken using a JEOL JXA-8200 'Superprobe'™ housed within Dalhousie University's Robert M. MacKay Electron Microprobe Lab. The EMPA has five wavelength-dispersive X-Ray spectrometers (WDS) with an additional energy-dispersive X-ray spectrometer (EDS). A voltage of 15 kv, amperage of 20 nA and beam size of 1 μm were used, with JEOL internal and *Probe for EPMA*™ external software for data collection.

Minor and trace element traverses were undertaken across larger veins at ~500-1000 μm apart and across smaller veins at ~ 100 μm apart (distances are approximate). Calibration with calcite, dolomite, diopside and olivine lab standards were interspersed every 25-40-point analyses. Element oxides of Ca^{2+}, Mg^{2+}, Fe^{2+}, and Mn^{2+} were analyzed, with Fe^{2+} and Mn^{2+} being the focus of this study and Ca and Mg being used to determine between different mineral species based on weight % oxide. Peak searching standards included calcite for Ca, dolomite for Mg, almandine garnet for Fe^{2+}, and pyrolusite for Mn^{2+}.

ZAF corrections were undertaken on all analyses. Data was compiled as wt. % oxides within a Microsoft Excel spreadsheet, and converted to ppm for comparison with other collected data. Carbon was not analyzed (given the carbon coating used in the

slide coating) giving anomalously low weight percent oxide totals for calcites of 45-50 wt.% (55 wt.% expected within the standard). However, values within this range were considered relatively accurate given that the ratio of Ca and C within carbonates is near 1:1, CaO is expected to make up the majority of the remaining oxides present, and minor phases of Fe^{2+}/Mn^{2+} rich oxides may lower the overall CaO count expected in pure calcites. Silicate (SiO_2) rich areas nearing 100 wt.% and MgO rich areas nearing 30 wt.% were used to distinguish between calcite, silicate, and dolomite species, with the latter generally averaging ~30 wt.% CaO. Analyses that exhibited >10 wt.% CaO from the calcite standard were also excluded, as too many impurities might be present to analyze versus the predominant calcite phase. Accuracy of the data was also assessed, with elemental wt.% measuring <99 wt.% lower detection limit for each element being excluded from analysis due to high data uncertainties.

3.2.5 C & O Stable Isotope Analysis

Locations of interest for stable isotope analysis were determined based upon textural and CL variation observed within the calcite veins. Isotopic analyses were conducted on the polished thick section from which the thin sections were cut. Powders were drilled using a Merchantek micromill and placed in clean glass vials. High-pressure air was used to remove calcite powder from the mill between drill runs in order to prevent cross contamination.

Twenty-One ^{13}C and ^{18}O stable isotope analyses were processed at the laboratories of the Scottish Universities Environmental Research Centre (SUERC), and fifteen more were processed at Memorial University Newfoundland's TERRA Stable Isotope Lab using a DeltaVPlus isotope ratio mass spectrometer (IRMS) equipped with a Thermo Electron GasBench II unit. In both processes, approximately 0.2mg of powdered pure carbonate was inserted into the bottom of a 12ml round-bottomed vial and covered with Exetainer screw caps with pierceable septa. The vials were placed in a heated sample holder at 50 ^{o}C. Using the GC Pal Autosampler, the vials were flushed with UHP-grade He gas for 8 min using a double-holed needle connected by tubing to the gas source. Samples were then injected with approximately 0.05 ml of phosphoric acid (100%) manually using a syringe and needle. A minimum of 1 h was allowed for

samples to react. For impure carbonate material, a larger volume of acid was injected into the sample vial, dependent upon sample size.

The Gas Chromatography (GC) Pal was used to sample the headspace of each vial using a double-holed needle flushed with UHP grade He gas. This He/sample gas mixture from the vial was carried through fused glass capillary tubing into the GasBench II, passing through a Nafion® drier. The dried gas goes through an 8-port switching valve with a 50 µl sampling loop. Using the sampling loop, portions of the sample gas were injected onto a 30 m x 0.32 mm GS-Q fused silica capillary GC column held at 50°C to separate the desired CO_2 gas from any other gases. The gas stream, containing the CO_2 sample gas, then passed through an additional Nafion® drier before being carried by He carrier gas into a Thermo Electron DeltaVPlus isotope ratio mass spectrometer (MS) via an open split interface. The open split tube allowed a small portion of the sample gas mixture to enter into the MS source via a fused glass capillary. Eight aliquots of sample gas were injected for each sample analysis. Another open split tube in the GasBench II allowed for the injection of the CO_2 reference gas into the source in between sample runs. Three different reference materials (RM) of known isotopic composition were included throughout each run and were treated to the same processes as the unknown samples.

ISODAT 3.0 software was used to measure ratios of m/z between mass 45/44 and 46/44, with values assigned to reference peaks in each analysis for comparison with the sample peaks to determine a “raw” isotope ratio for the sample. The “raw” isotope ratios determined by the software were calibrated offline using Microsoft Excel. Two RMs with high and low isotope ratios were used to calibrate (or normalize) the data, while the third was used as a check standard. The calibrated data were then imported into the LIMS for Light Stable Isotopes database (A. Pye, email message, Jan. 8, 2018).

3.2.6 Laser Ablation Analysis

3.2.6.1. U-Pb LA-ICPMS

U-Pb calcite analyses are based on the procedures outlined by Roberts et al. (2016) and were undertaken by Dr. Nick Roberts at the BGS NERC Isotope Geosciences Laboratory in Nottingham, UK. The analyses were collected by a Nu

Instruments single collector Attom Laser Ablation Inductively Coupled Plasma Mass Spectrometer (LA-ICPMS) coupled to a New Wave Research (ESI) NWR193UC laser ablation system equipped with a TV2 ablation cell. The thick sections corresponding to samples JV17-1a, JV17-2, and JV17-5 (not included in this study) were analyzed using 100 μm static spot, ablated for 30 s at 10 Hz with a fluence of 7–8 J/cm. The depth of the ablation pit using these settings was ~45 μm. Normalization of data utilized a standard-sample bracketing Protocol, with NIST614 glass being used for mass fractionation correction of Pb isotope ratios. These are estimated to be ca. 0.7 % for the $^{207}Pb/^{206}Pb$ ratio. The WC-1 calcite standard was then used for correction of U-Pb ratios (defined as a standard within Roberts et al. 2016). Data was reduced by Roberts using the Time Resolved Analysis (TRA) functionality in Nu Instruments' Attolab software, with normalization and uncertainty propagation calculated off-line using an in-house Microsoft Excel spreadsheet.

3.2.6.2 Trace & REE LA-ICPMS

Laser ablation studies (following the form of those undertaken by Sturrock et al. 2017 and Jochum et al. 2012) were undertaken at the Dalhousie Laboratory for Experimental High Pressure Geological Research. Minor and trace REE analyses were undertaken on the polished thin sections of samples JV17-1a, JV17-2, JV17-6, JV17-9, JV17-10, JV17-11, and JV17-12 using a New Wave Research frequency quintupled laser operating at 213 nm, coupled to a quadrupole mass spectrometer (PQ Excell or Thermo X-series) with He flushing. The analyses occurred as both linescans and spot analyses, with a 100μm spot size, ablated at 4-5 Hz with a 20% total energy. Concentrations of ^{43}Ca, ^{55}Mn, ^{57}Fe, ^{85}Rb, ^{86}Sr, ^{87}Sr, ^{89}Y, ^{137}Ba, ^{139}La, ^{140}Ce, ^{141}Pr, ^{146}Nd, ^{147}Sm, ^{153}Eu, ^{157}Gd, ^{159}Tb, ^{163}Dy, ^{165}Ho, ^{166}Er, ^{169}Tm, ^{172}Yb, and ^{175}Lu were measured in blocks of sixteen analyses, with two NIST 610 bounding each block for a total of 20 analyses per run. Total run times were 140 s, with 20 s laser warm-up, 60 s ablation, and 60 s He-gas flushing time. However, due to calcite burn through, many analyses were between 20-30 s in order to prevent damage to the slide.

Data reduction was done off-line using Igor Pro and Iolite. Base levels were determined through ^{43}Ca peak analysis making sure to avoid anomalous intensities but also including washout periods. Analytical drift was addressed by running a linear

regression through average ^{43}Ca intensities in the NIST610 runs before and after unknown analyses. The drift correction was employed in the Iolite calibration. REE values were normalized to chondrite data provided by McDonough & Sun (1995) using Microsoft Excel, following methods outlined in Rollinson (1993).

3.2.7 Clumped Isotope (Δ_{47}) Paleothermometry

Carbonate clumped isotope (Δ47) measurements were carried out by Dr. Ian Winkelstern in the Isotopologue Paleosciences Laboratory at the University of Michigan, Ann Arbor. Samples were powdered using a dental drill. For Δ_{47} analysis, ~ 8 mg of sample powder was reacted in an automated preparation line previously described in Henkes et al., (2014). Carbonate powders were reacted under vacuum with 104% phosphoric acid at 90 °C for 10 min. Vapour-phase water generated during the reaction was separated from the produced CO_2 using liquid nitrogen swapped out an ethanol–liquid nitrogen mixture held at −85 °C. The water remained frozen while the CO_2 was passed through a Poropak Q chromatography trap held at −20 °C. The purified CO_2 was measured using a Nu Instruments Perspective isotope ratio mass spectrometer in dual inlet mode, with a measurement time of c. 2 h. All analyses were run as triplicates. Masses 44–49 were measured. Carrara marble and an in-house carbonate standard were used to verify the results.

All carbonate clumped isotope (Δ_{47}) values in this study are presented on an absolute reference frame, also termed a 'carbon dioxide equilibrium scale' or CDES, which empirically corrects for instrumental nonlinearities and changes in the ionization environment during mass spectrometry (Dennis et al. 2011; MacDonald et al. 2017). This reference frame was established by periodically analyzing aliquots of CO_2 that were isotopically equilibrated at 25 or 1000 ^{o}C (for details see Dennis et al., 2011). Temperatures were calculated from Δ_{47} using the empirical "high temperature" Δ_{47} - temperature relationship from Bonifacie et al. (2017)

- Chapter 4: RESULTS -

4.1 Field Observations

Vein growth primarily occurred within MVF volcanic rocks, which contained abundant amygdale filling and minor interactions with sedimentary packages in the form of peperites and other sedimentary remnants reworked by the volcanic activity (Figure 4). Most veins appear to be randomly oriented, with abundant stock work veining present.

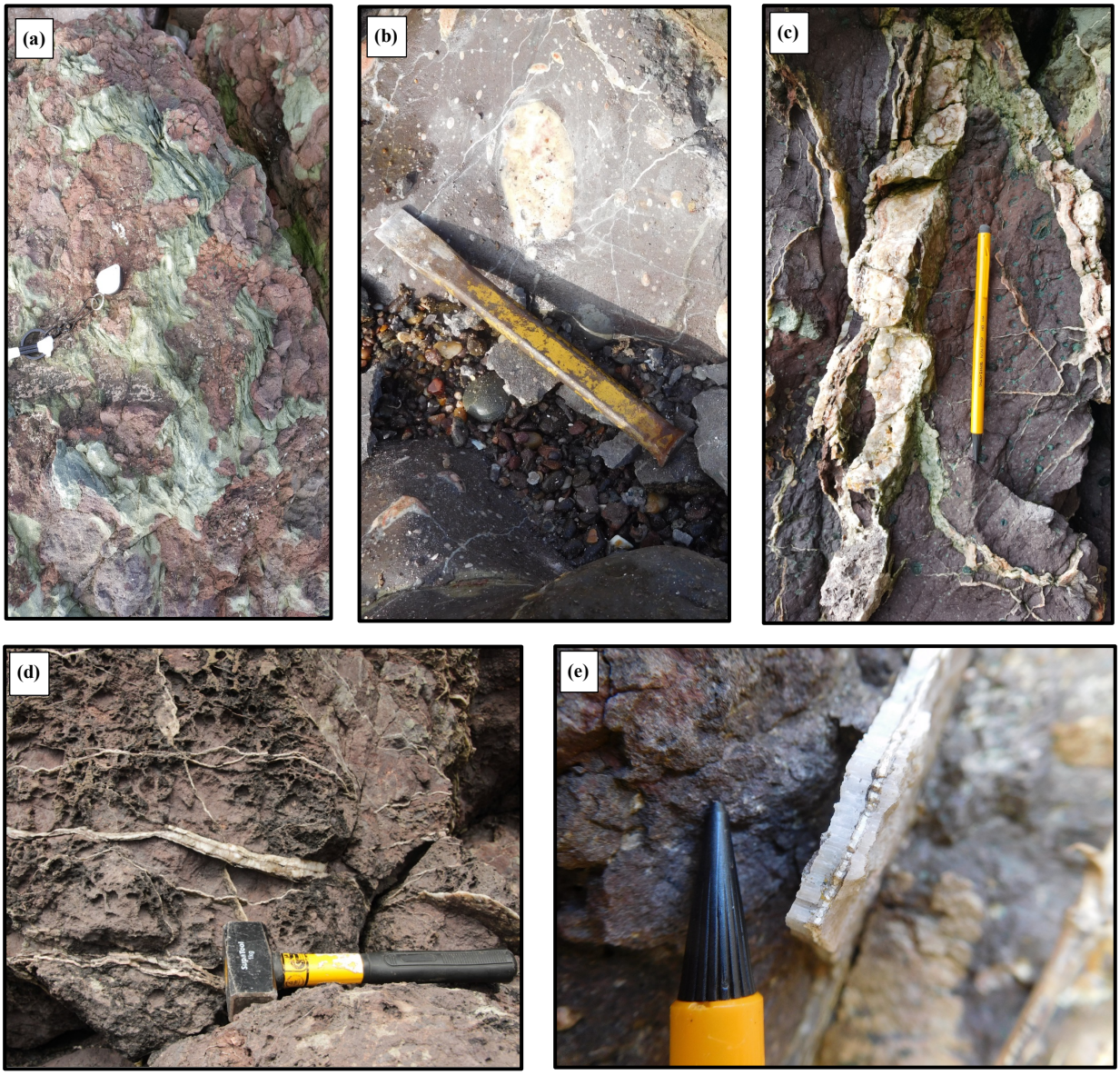

Figure 4. (a) MVF lavas with interbedded sedimentary layers. (b) abundant amygdales within eroded MVF bedrock outcrops (c), (d) & (e) abundant stock work and disseminated carbonate (calcite) veining with various sizes and orientations.

4.2 Optical & Cathodoluminescent Analyses

4.2.1 Carbonate Veins

The veins analyzed within this study varied from >50 mm in width to less than 5 mm (Figures 5 – 10). Primary vein formation is along a singular opening (JV17-1a, JV17-2, JV17-9), although some veins also occur as a bundle of sub parallel veins (JV17-12). Within these veins, multiple forms of calcite growth were recognized including bladed (JV17-1a) and toothy (JV17-2, JV17-9) calcites along host rock contacts (Figure 5 (a)), while euhedral, scalenohedral, and blocky crystals making up the bulk of most vein matrices (JV17-1, JV17-2, JV17-12) (Figure 5 (b)). Crosscutting relationships and alteration are readily observed in JV17-1a, where a primarily syntaxial, bedrock growth phase is crosscut by a secondary, anhedral growth phase, and in JV17-11, where a stretched vein is crosscut by an iron rich vein. Multiple phases are also evidenced by bedrock fragments and remnant calcite crystal growth along these fragments that have been sealed within the vein during subsequent vein sealing (JV17-1a, JV17-12) (Figures 7, 11).

JV17-11 contains the only formation of stretched beef-veining (appearing similar to beef tendons), progressing from stretched/bladed crystals with vein opening (Figure 10), although other samples not included within this study were also observed to have significant beef veining. Minor veins are prevalent in many of the samples (JV171a, JV17-2, JV17-9, JV17-11), predominantly sealed with fine, euhedral calcite crystals only a few mm in size. Accessory minerals (quartz and chlorite) are visible along the vein-bedrock contacts, while reddish sutures are visible during the final stage of vein formation/closure in JV17-1a and JV17-2, consisting primarily of iron oxides and other rare carbonate phases (Figures 5, 6). These suture-defined vugs are filled with predominantly cloudy, anhedral calcites. Despite the variations in texture, only JV17-11 exhibits antitaxial vein growth.

4.2.2 Amygdales

Abundant nodules were found within the andesitic basalt host-rocks. These range in size from less than 10 mm in width/ circumference (JV17-6) to more than 100 mm in circumference (JV17-10) (Figure 9) Amygdale fill material is primarily composed of calcite, with concentric zonation of quartz along the bedrock interface, and common

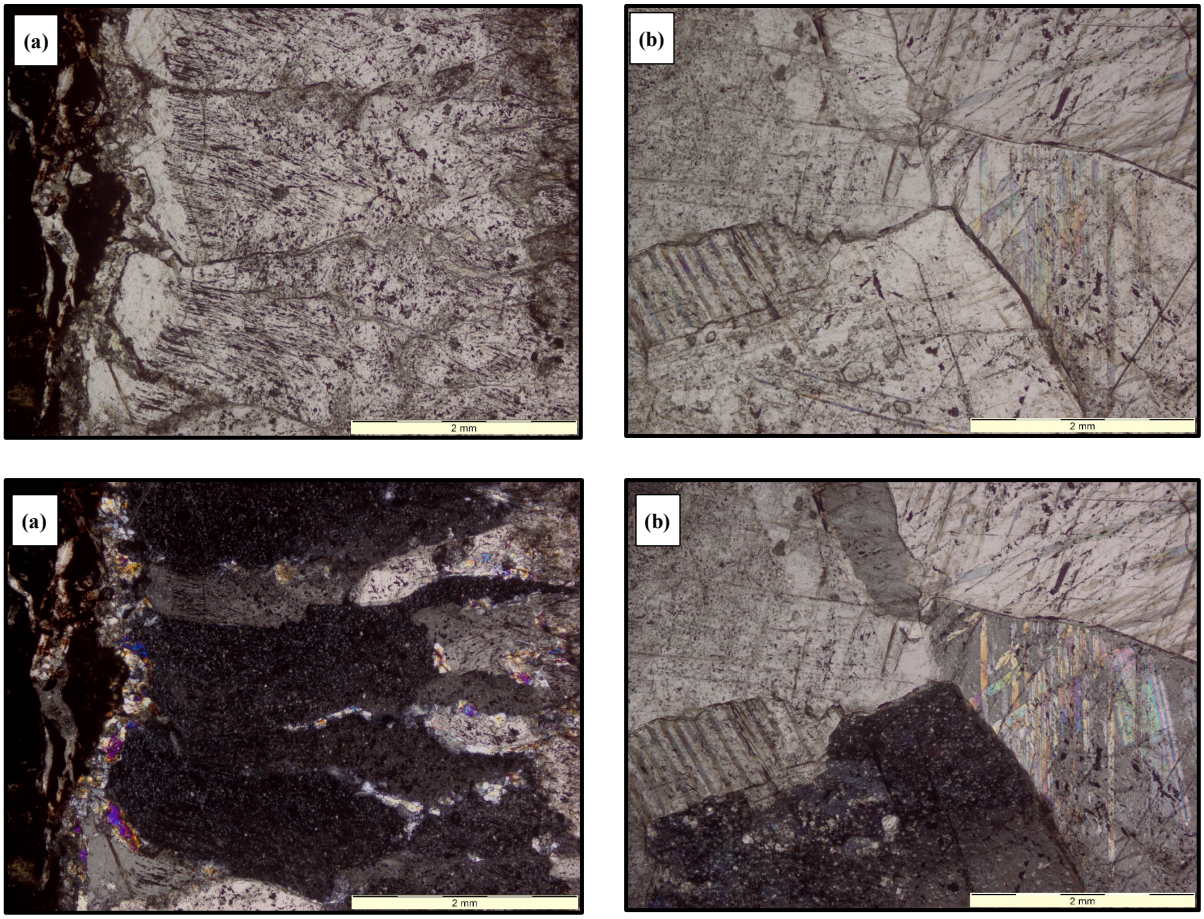

Figure 5. (a) stretched/ bladed syntaxial growth along the bedrock interface of JV17-1a showing uniform growth direction from cross polarized extinction (top – PPL, bottom XPL). (b) euhedral, blocky/ equant growth within the matrix of JV17-2 showing variable growth direction from cross polarized imagery (top – PPL, bottom XPL).

chlorite and formation zeolites in some larger amygdales (JV17-10). Amygdale material is often crosscut/ fragmented by the formation of calcite veining.

4.2.3 Cathodoluminescence (CL) Microscopy

Figures 6-11 show collated CL imagery for samples JV17-1a, JV17-2, JV17-9, JV17-10, JV17-11, and JV17-12, respectively. Minor variations in CL can be seen within the larger individual euhedral - anhedral blocky crystals that make up the bulk of the vein matrix in JV17-1a and JV17-2. However, CL signatures are generally uniform across individual veins and amygdales despite textural variation, with primary excitation associated with calcite cleavage planes and extinction (dark pink-purple in colour) associated with the vein closure vugs/ areas of high Fe^{2+}/Mn^{2+} oxide concentration.

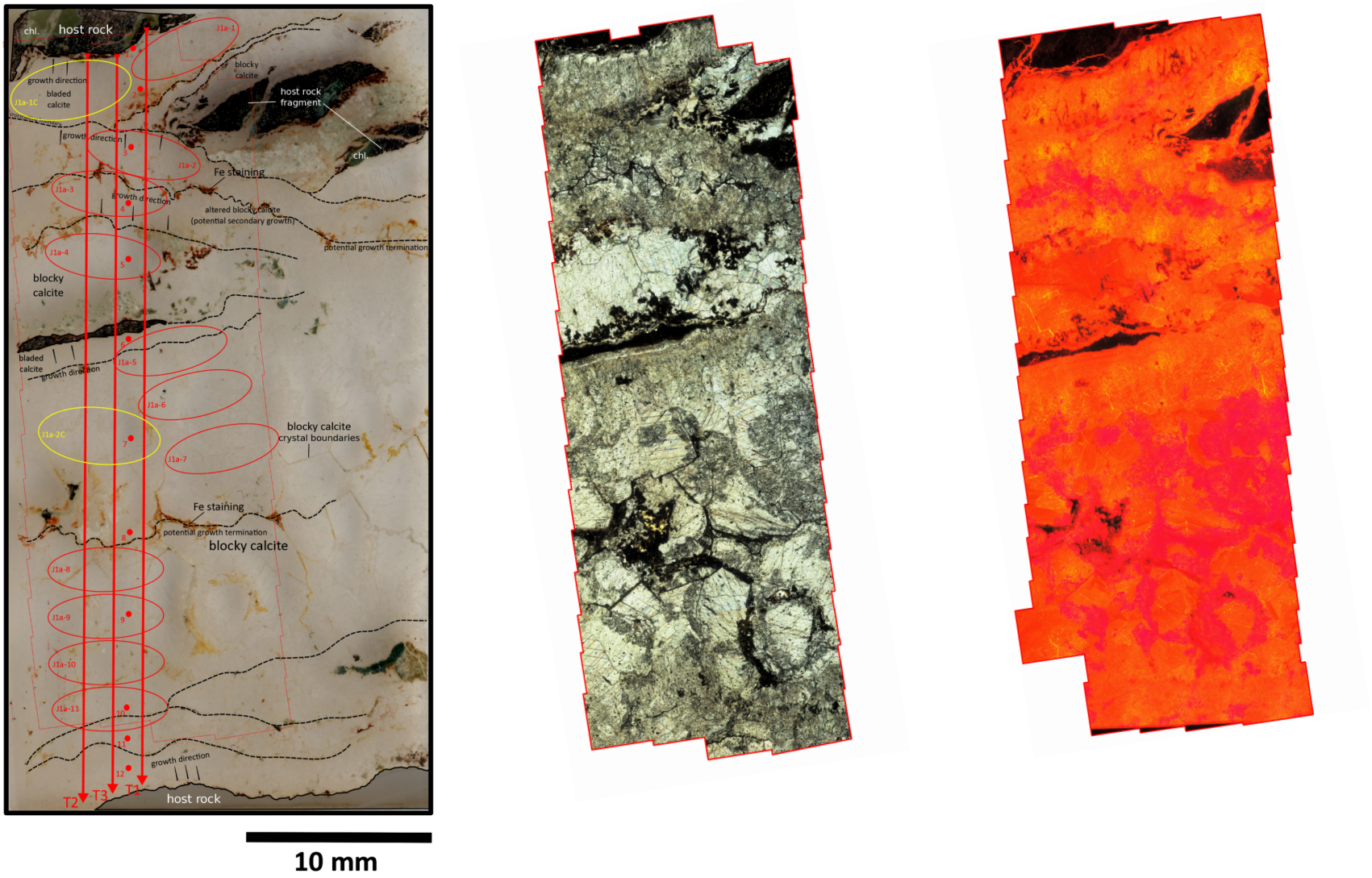

Figure 6. Slide (left), plane polarized (middle), and CL (right) imagery for Sample JV17-1a, showing the locations of analyses, as well as interpretation of vein growth phases and growth directions.

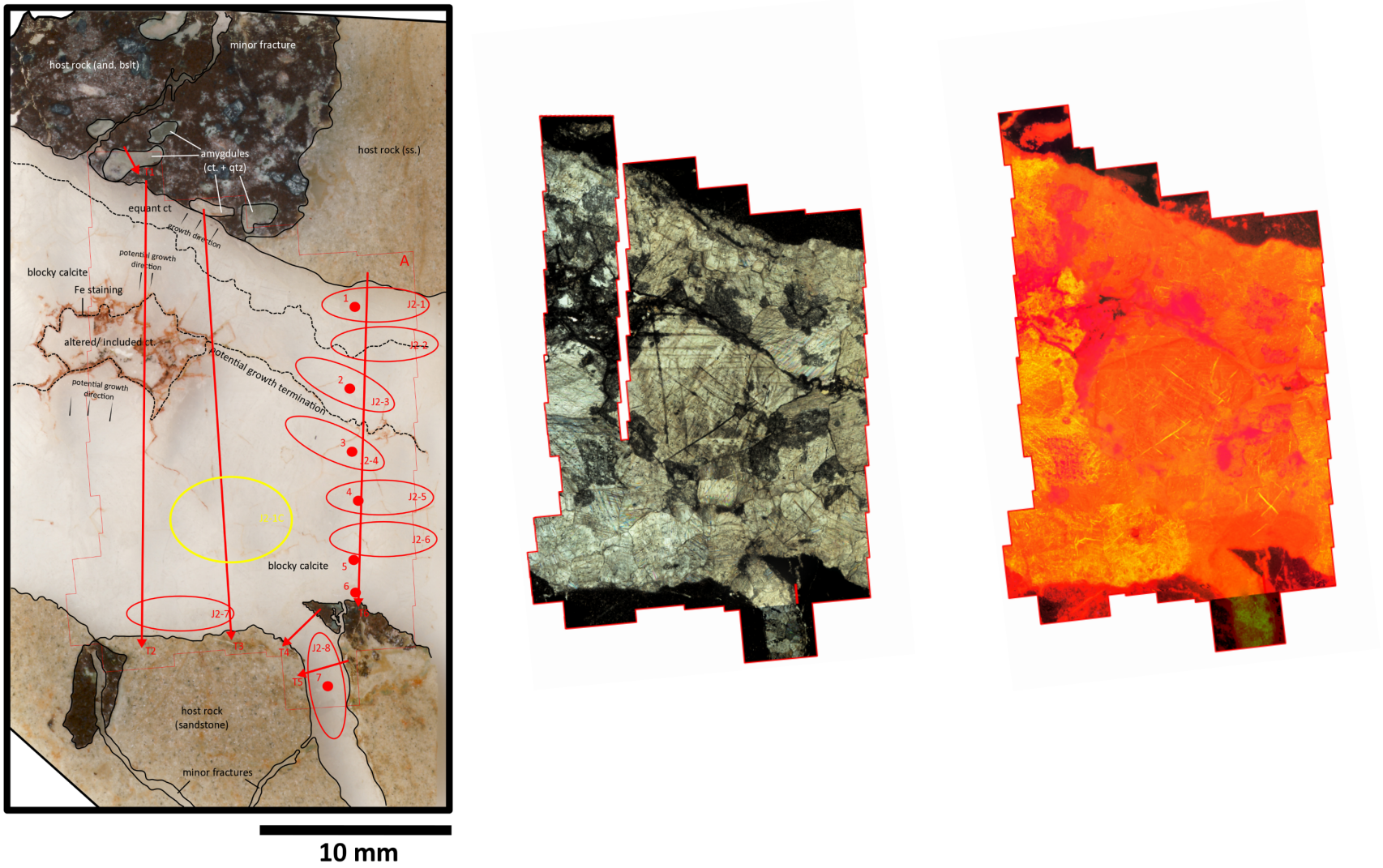

Figure 7. Slide (left), plane polarized (middle), and CL (right) imagery for Sample JV17-2, showing the locations of analyses, as well as interpretation of vein growth phases and growth directions.

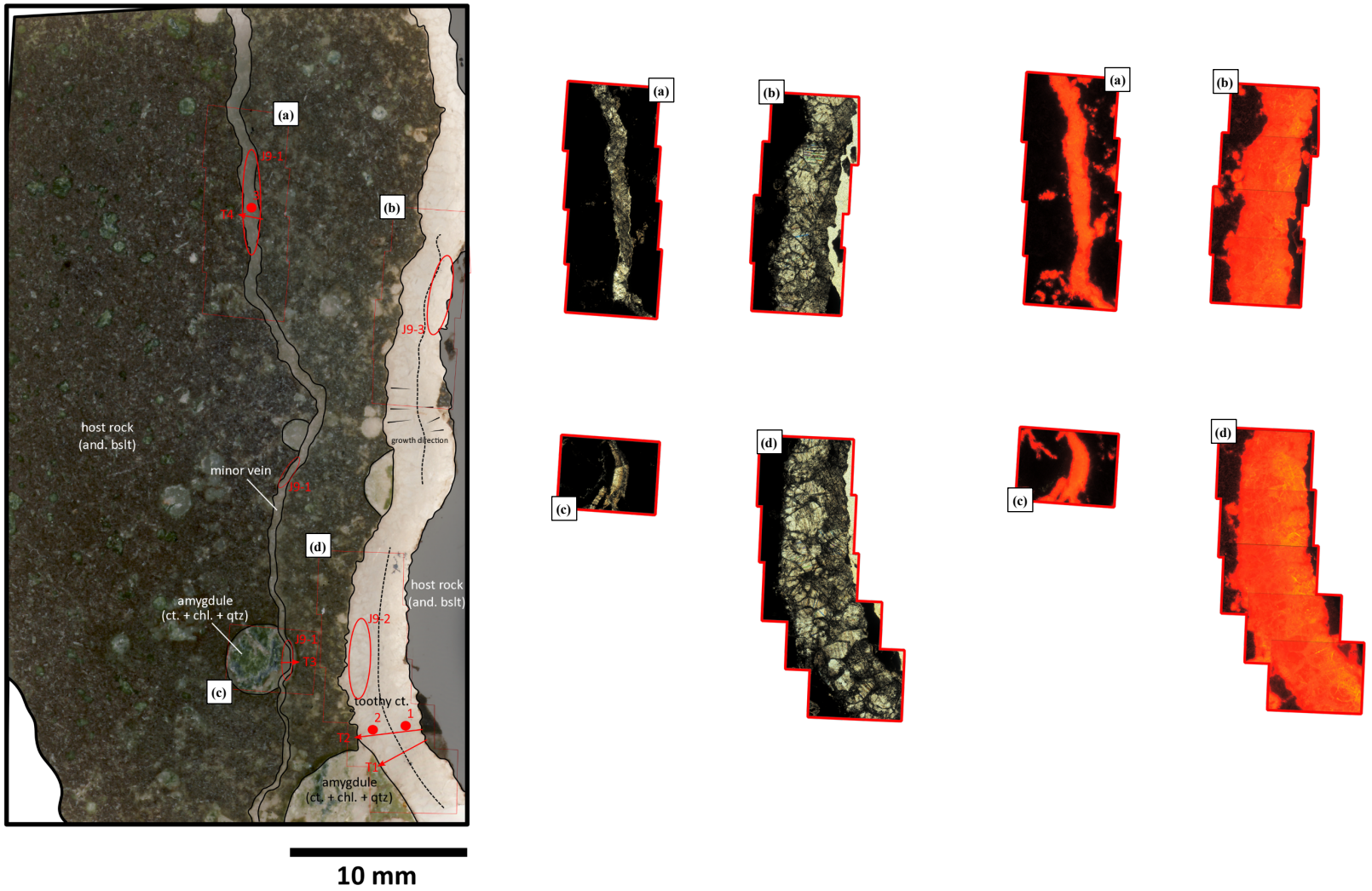

Figure 8. Slide (left), plane polarized (middle), and cathodoluminescent (right) imagery for Sample JV17-9, showing the locations of analyses, as well as interpretation of vein growth phases and growth directions.

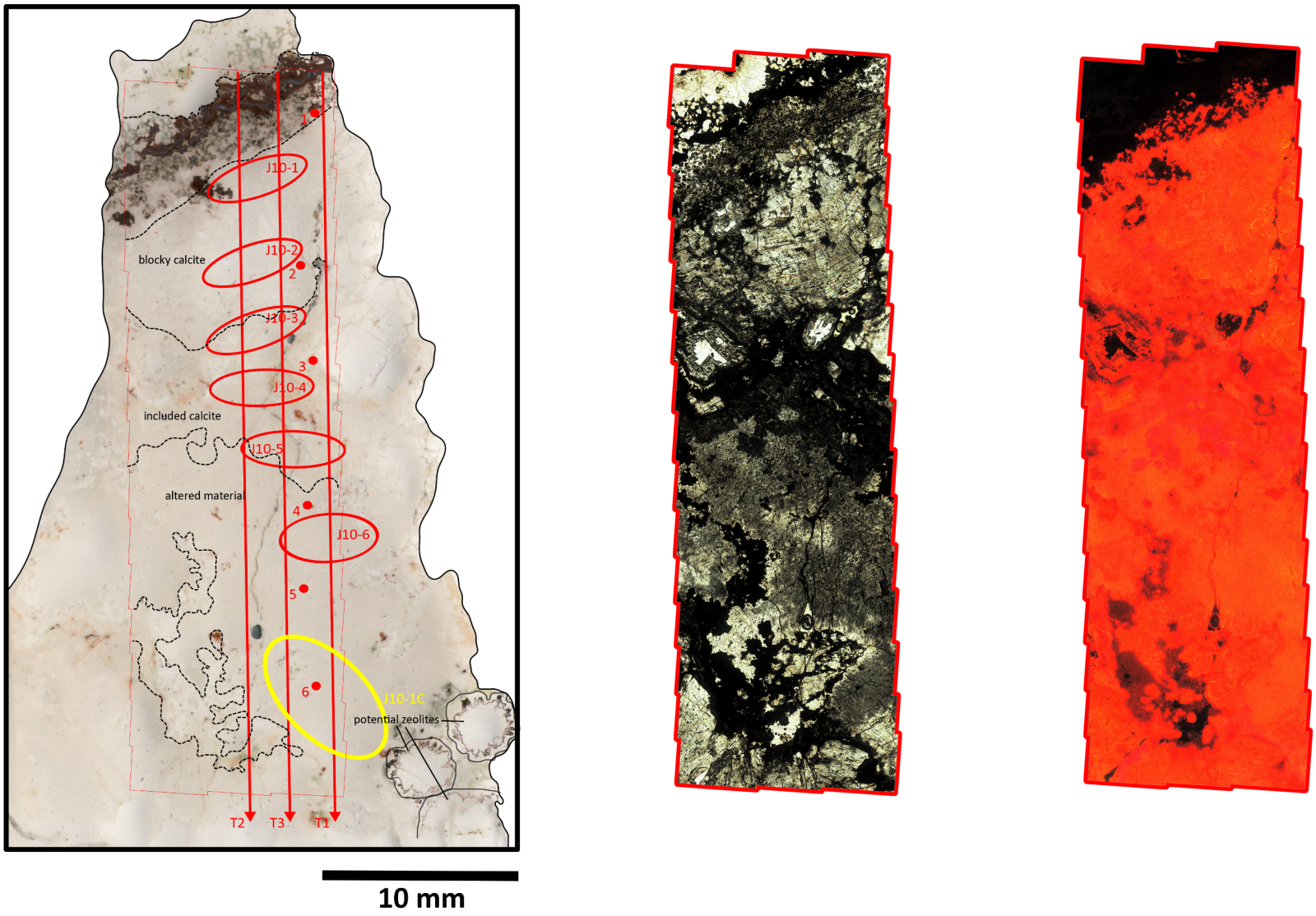

Figure 8. Slide (left), plane polarized (middle), and cathodoluminescent (right) imagery for Sample JV17-10, showing the locations of analyses, as well as interpretation of vein growth phases and growth directions.

Figure 10. Slide (left), plane polarized (middle), and cathodoluminescent (right) imagery for Sample JV17-11, showing the locations of analyses, as well as interpretation of vein growth phases and growth directions.

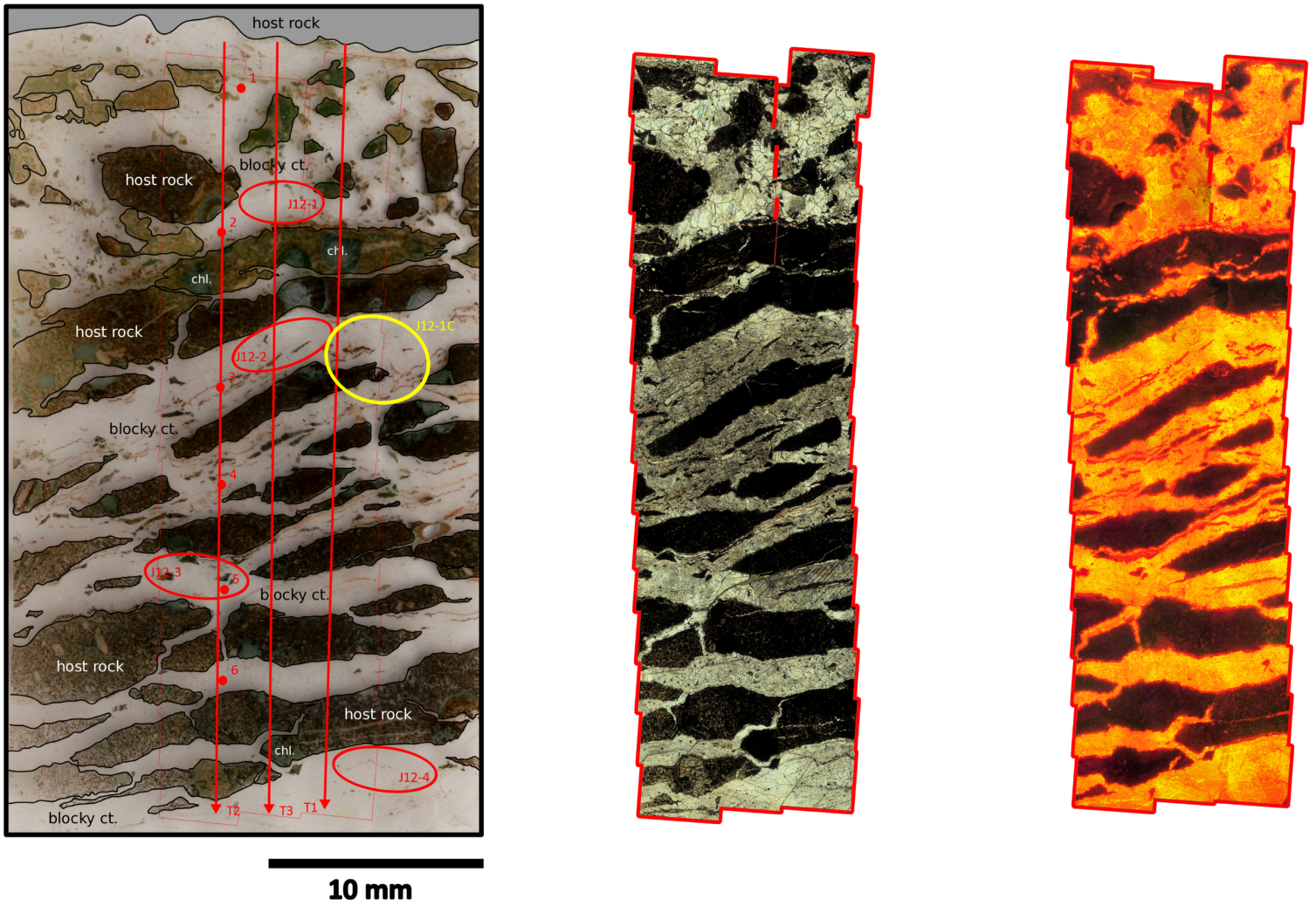

Figure 11. Slide (left), plane polarized (middle), and cathodoluminescent (right) imagery for Sample JV17-12, showing the locations of analyses, as well as interpretation of vein growth phases and growth directions.

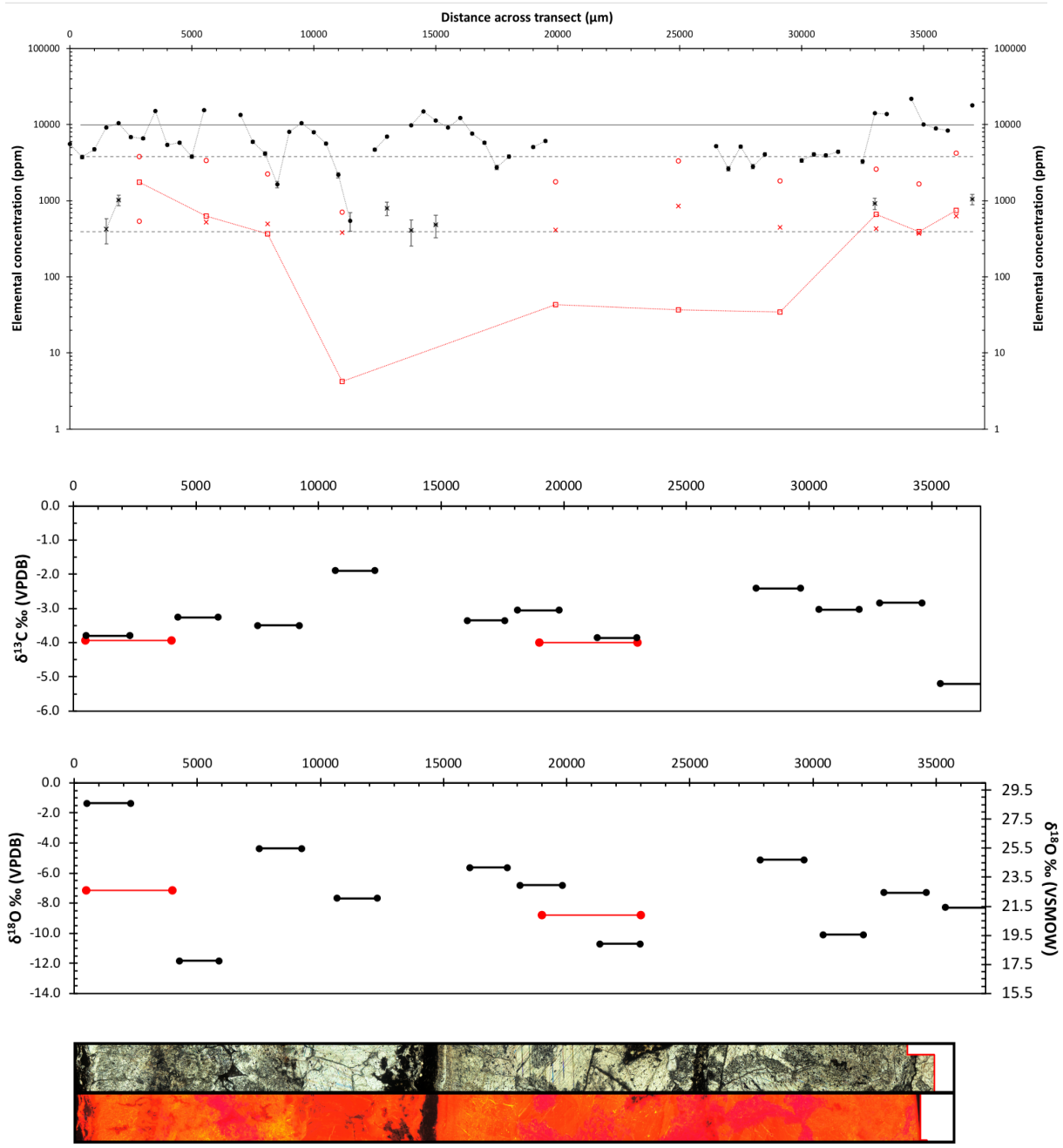

Figure 12. Electron microprobe analyses for JV17-1a, Transect 3 (top). Black Fe^{2+} (x) and Mn^{2+} (o) probe values with comparison to red LA-ICPMS analyses with ΣREE in red squares. Dark solid line = average Mn^{2+} probe value for nodules studied (JV17-6 and JV17-2, n=87) with lighter solid line as the upper 1σ value for same analyses. Black Dashed line = average Fe^{2+} probe value for nodules studied (n=35) with lighter dashed line as the upper +/-1σ values for same analyses. Comparison to stable isotope data (middle) and PPL and CL imagery (bottom) from the same transect.

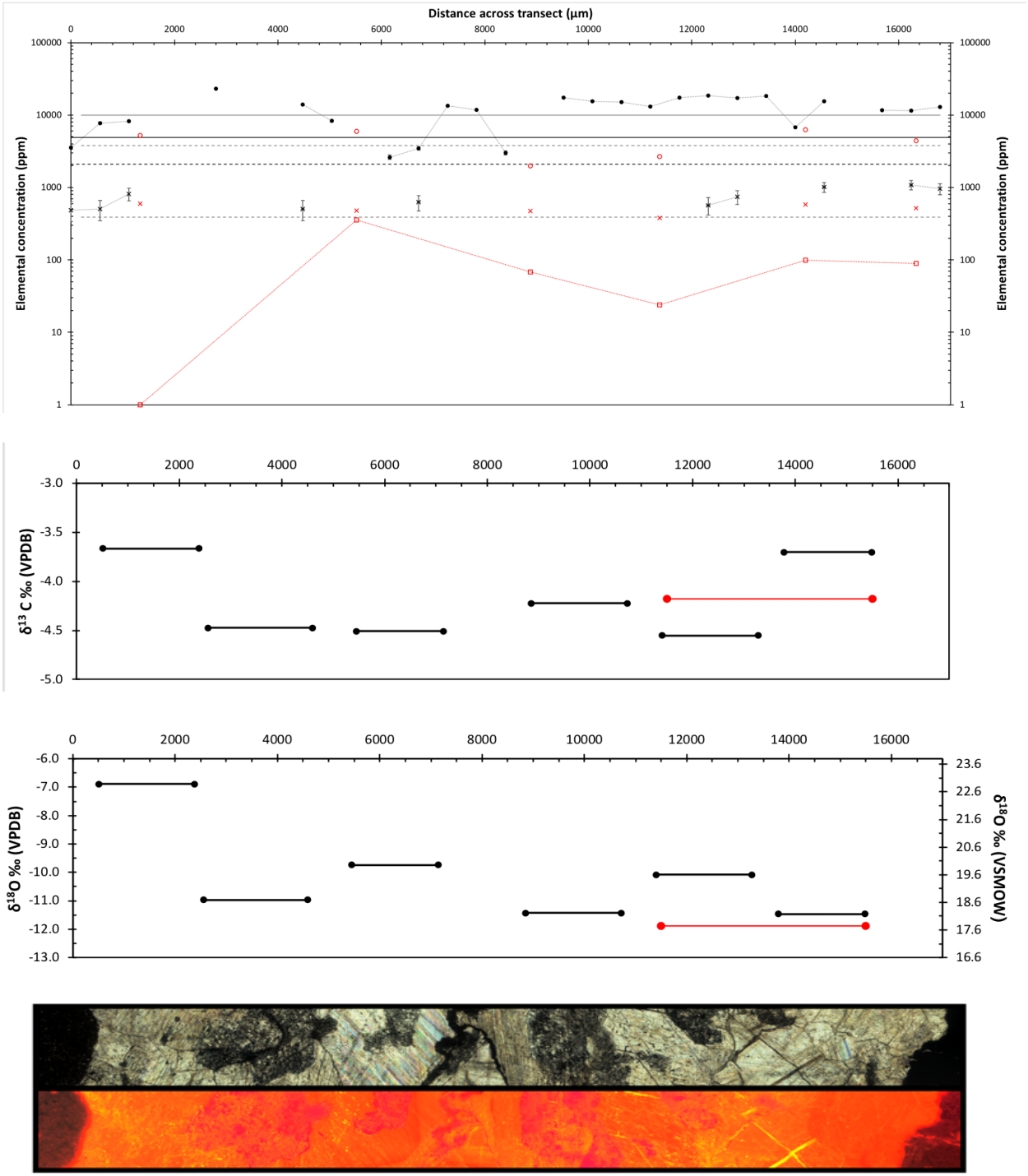

Figure 13. Electron microprobe analyses for JV17-2, Transect 6 (top). Black Fe^{2+} (x) and Mn^{2+} (o) probe values with comparison to red LA-ICPMS analyses with ΣREE in red squares. Dark solid line = average Mn^{2+} probe value for nodules studied (JV17-6 and JV17-2, n=87) with lighter solid line as the upper 1σ value for same analyses. Black Dashed line = average Fe^{2+} probe value for nodules studied (n=35) with lighter dashed line as the upper +/-1σ values for same analyses. Comparison to stable isotope data (middle) and PPL and CL imagery (bottom) from the same transect.

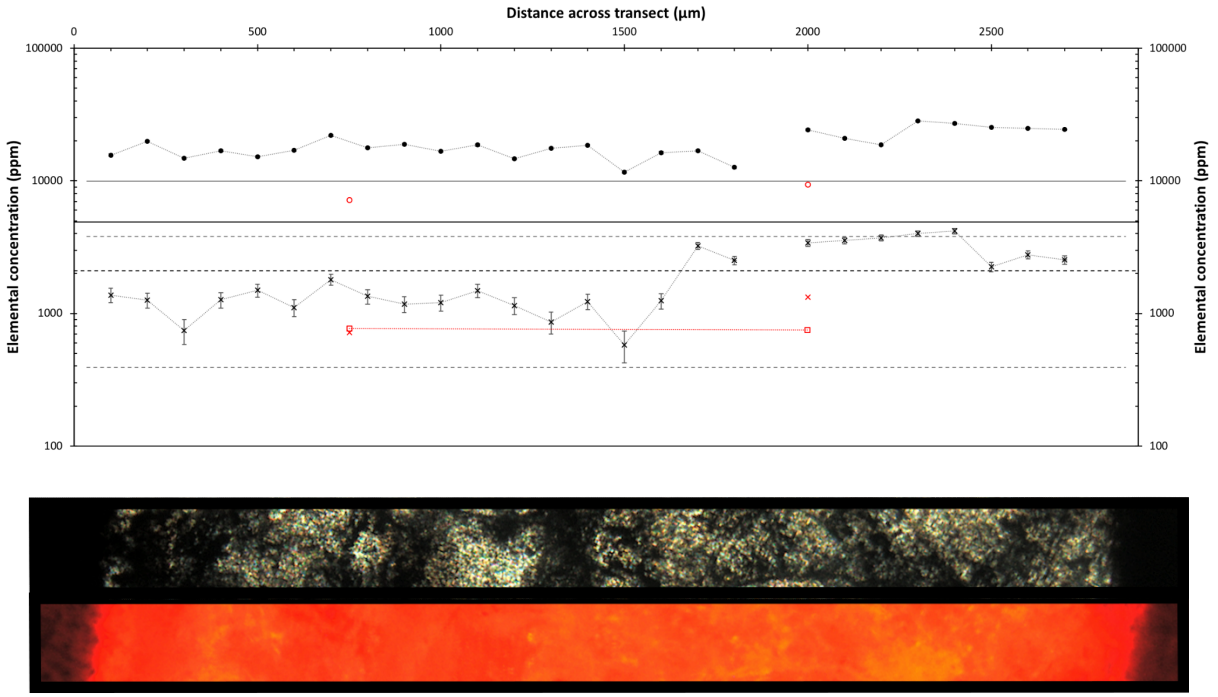

Figure 14. Electron microprobe analyses for JV17-9, Transect 2 (top). Black Fe^{2+} (x) and Mn^{2+} (o) probe values with comparison to red LA-ICPMS analyses with ΣREE in red squares. Dark solid line = average Mn^{2+} probe value for nodules studied (JV17-6 and JV17-2, n=87) with lighter solid line as the upper 1σ value for same analyses. Black Dashed line = average Fe^{2+} probe value for nodules studied (n=35) with lighter dashed line as the upper +/-1σ values for same analyses. Stable Isotope Data point JV17-2 covers most of the vein material. Comparison to PPL and CL imagery (bottom) from the same transect.

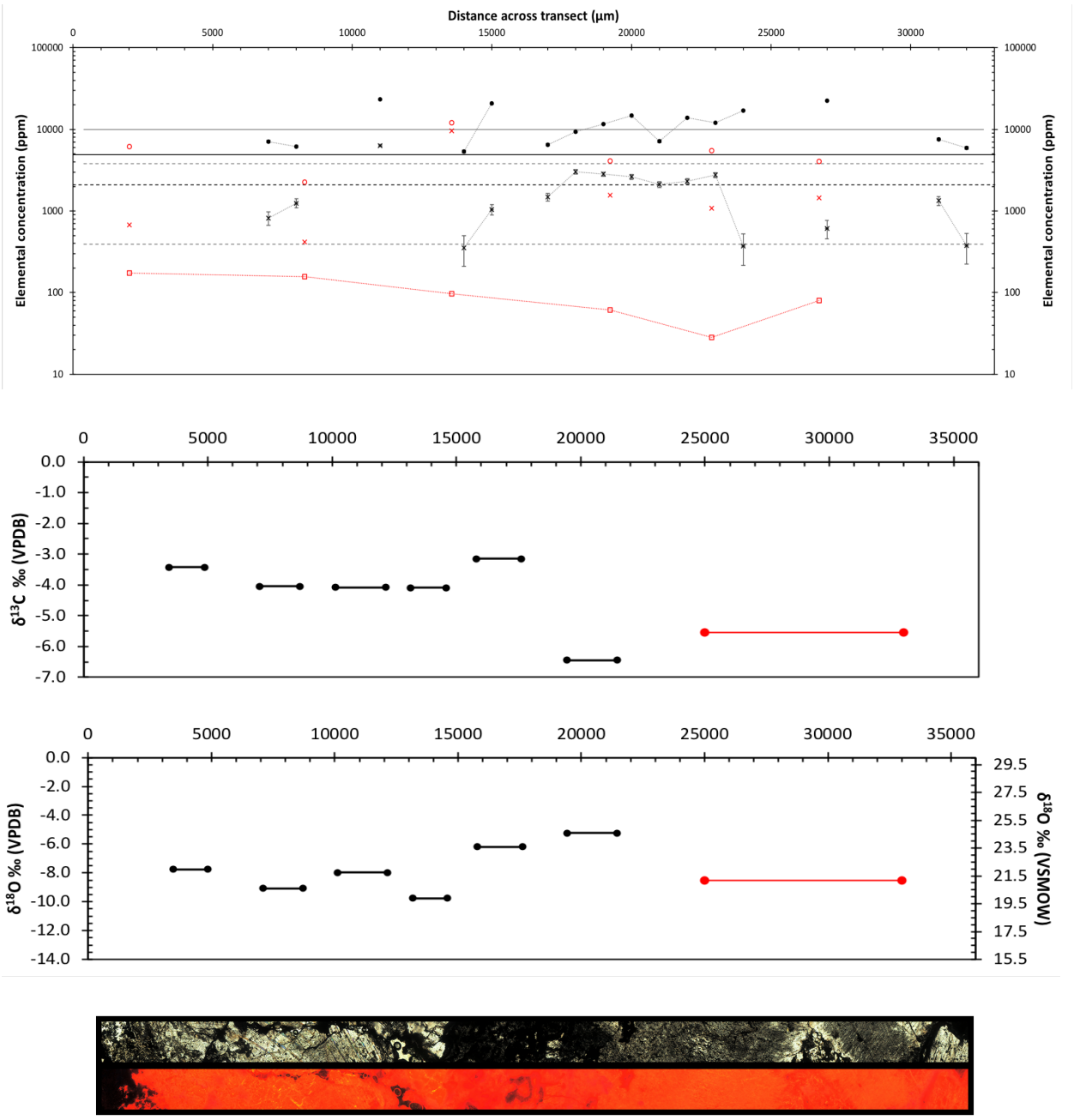

Figure 15. Electron microprobe analyses for JV17-10, Transect 2 (top). Black Fe^{2+} (x) and Mn^{2+} (o) probe values with comparison to red LA-ICPMS analyses with ΣREE in red squares. Dark solid line = average Mn^{2+} probe value for nodules studied (JV17-6 and JV17-2, n=87) with lighter solid line as the upper 1σ value for same analyses. Black Dashed line = average Fe^{2+} probe value for nodules studied (n=35) with lighter dashed line as the upper +/-1σ values for same analyses. Comparison to stable isotope data (middle) and PPL and CL imagery (bottom) from the same transect.

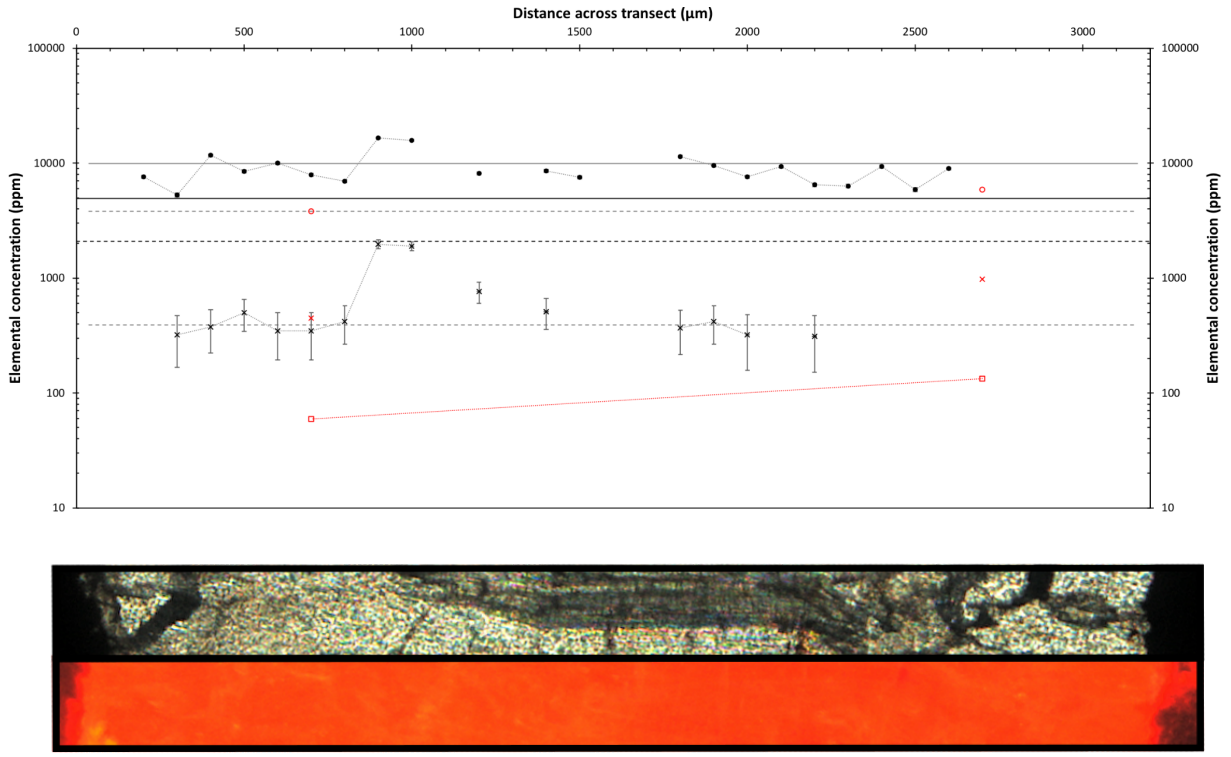

Figure 16. Electron microprobe analyses for JV17-11, Transect 1 (top). Black Fe^{2+} (x) and Mn^{2+} (o) probe values with comparison to red LA-ICPMS analyses with ΣREE in red squares. Dark solid line = average Mn^{2+} probe value for nodules studied (JV17-6 and JV17-2, n=87) with lighter solid line as the upper 1σ value for same analyses. Black Dashed line = average Fe^{2+} probe value for nodules studied (n=35) with lighter dashed line as the upper +/-1σ values for same analyses. Stable isotope data point JV17-11-3 covers the first half of the vein, including both phases of growth. Comparison to PPL and CL imagery (bottom) from the same transect.

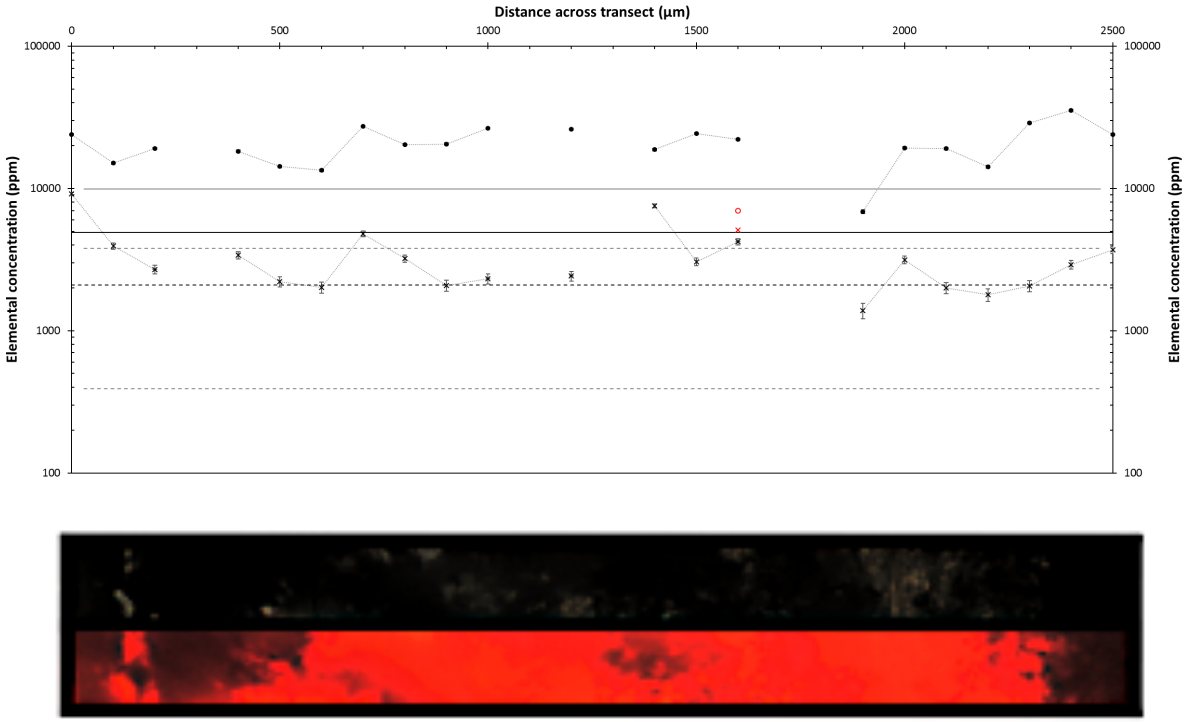

Figure 17. Electron microprobe analyses for JV17-11, Transect 2 (top). Black Fe^{2+} (x) and Mn^{2+} (o) probe values with comparison to red LA-ICPMS analyses with ΣREE in red squares. Dark solid line = average Mn^{2+} probe value for nodules studied (JV17-6 and JV17-2, n=87) with lighter solid line as the upper 1σ value for same analyses. Black Dashed line = average Fe^{2+} probe value for nodules studied (n=35) with lighter dashed line as the upper +/-1σ values for same analyses. Stable isotope data point JV17-11-2 covers most of the transect. Comparison to PPL and CL imagery (bottom) from the same transect.

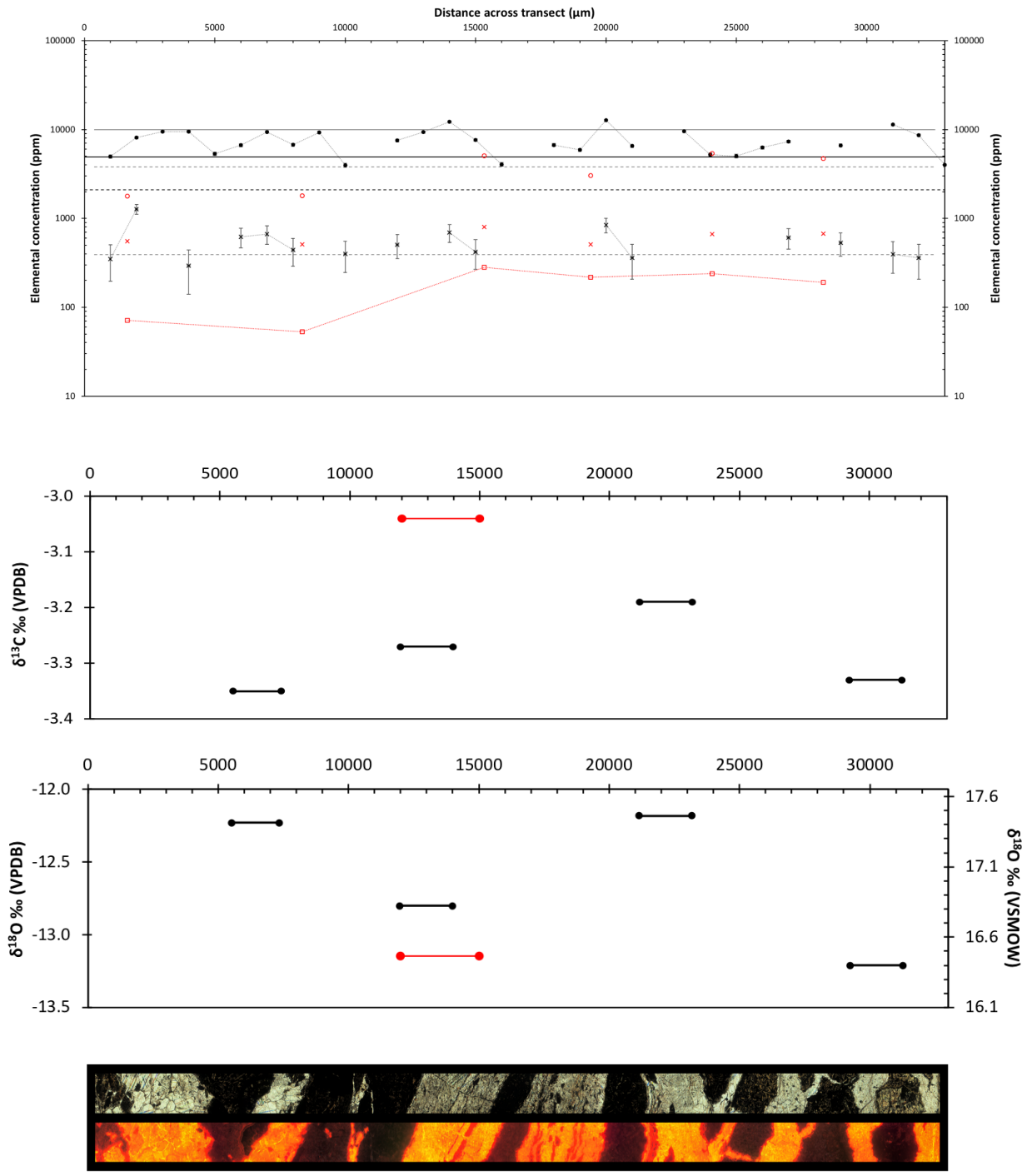

Figure 18. Electron microprobe analyses for JV17-12, Transect 2 (top). Black Fe^{2+} (x) and Mn^{2+} (o) probe values with comparison to red LA-ICPMS analyses with ΣREE in red squares. Dark solid line = average Mn^{2+} probe value for nodules studied (JV17-6 and JV17-2, n=87) with lighter solid line as the upper 1σ value for same analyses. Black Dashed line = average Fe^{2+} probe value for nodules studied (n=35) with lighter dashed line as the upper +/-1σ values for same analyses. Comparison to stable isotope data (middle) and PPL and CL imagery (bottom) from the same transect.

4.3 Minor & Trace REE Analyses

Twenty vein/nodule microprobe transects were undertaken, a selection of which can be seen in in Figures 11 to 18 with corresponding LA-ICPMS, stable isotope data, and CL imagery (see Appendix 1 for raw data from all EMPA transects and LA-ICPMS analyses). Within both forms of analysis, concentrations of Mn^{2+} and Fe^{2+} varied strongly across individual veins and amygdales – often by an order of magnitude. Mn^{2+} concentration ranged between ~500 ppm and ~40000 ppm, while most values occurred within the 5000-15000 ppm range (Table 2). It was not uncommon (even within amygdale samples) for Mn^{2+} concentrations to fluctuate strongly over short distances (500-1000μm) or individual growth phases, although minor veins generally had lower magnitudes of fluctuation than major veins. Typical Fe^{2+} values for ranged between 100 and 5000 ppm range for both EMPA and LA-ICPMS analyses, with most values nearer to 1000 ppm within both veins and nodules. With the exception of JV17-1a and JV17-10, fluctuations in Fe^{2+} were of a lower magnitude between consecutive point analyses in comparison to those observed in Mn^{2+}. The largest magnitudes of Fe^{2+} seem to correspond to areas of significant staining noted in optical analysis, such as within JV17-11-T2 and JV17-1a, although this is by no means the rule across all samples. However, Fe^{2+} concentrations often fell near the lower limit of detection for the EMPA, reducing the number of accurate analyses per transect, and leaving large gaps that may obscure major trends in the data. Furthermore, where EMPA and LA-ICPMS analyses occurred within the same location, major differences resulted ~ 25% of the time, although the majority fall within error of each other.

Comparing vein and amygdule minor element concentrations, Mn^{2+} generally fell at or above the average determined from the multiple bedrock amygdule analyses (~4500 ppm - primarily from JV17-6), as did the values of JV17-10. Major veins (JV17-1a, JV17-12) consistently fall just above this average value, while minor veins (JV17-9-T2, JV17-11-T2) often exhibit Mn^{2+} concentration >1σ Mn^{2+} (~10000 ppm) determined by amygdale standardization. although some samples do not fit these generalizations (see JV17-2-T5 for a wider vein exhibiting >1σ Mn^{2+}, and JV17-11-T1 for a minor vein exhibiting less than average Mn^{2+} concentrations in comparison to amygdule standards). In comparison to the amygdule samples, vein-hosted Fe^{2+} appears to be

lower or equal to the defined average, with the exception of peaks reaching +1σ in JV17-9, JV17-10, and JV17-11) (Figures 12-18).

Total ΣREE decreases with increasing distance from the host rock in JV17-1a, but generally remain constant across other samples (Figures 12-18). These totals are highly controlled by LREE, which makes up the bulk of REE enrichment in all samples studied. When normalized to chondrite (using the values of McDonough and Sun, 1995), this enrichment is predominant, with a fairly constant decrease in LREE-HREE fractionation for most samples (ΣLREE/ ΣHREE ranging from 4 - 63). Deviations from this trend include slight HREE flattening in JV17-11. and slight depletion of LREE in JV17-2-2 (Figure 19). The other notable exception is analysis JV17-10-2, which follows the trend of other analyses but has a much more saw-tooth appearance. This is most likely due to user error, where the laser engaged in collection without the proper; this error may also be the reason why the Mn^{2+} and Fe^{2+} concentrations are lower than the neighbouring analyses. Finally, a strong negative Tm anomaly is visible in JV17-6-2. This anomaly occurred within an analytical block for which the standard values were deemed acceptable, and therefore was included analyses presented here. Furthermore, all other analyses experienced nearly identical Tm anomalies (Tm/Tm* = 0.07-0.09) when normalized to JV17-6-2, suggesting no Tm variation within the original samples and therefore allowing for the overall trend to be interpreted independently of this variation. However, an analytical artifact for this sample cannot be completely ruled out, although similar anomalies have been found in other studies (Uysal et al. 2007).

The deviation of normalized Ce and Eu values from those anticipated in a mineral is known as a Ce or Eu anomaly. This is expressed as Ce/Ce*, or Eu/Eu*, where Ce* and Eu* are the predicted normalized values, based on the normalized values of the adjacent REEs (Barker & Cox 2011). Cerium anomalies range from 0.75 (slightly negative) to 1.17 (slightly positive), with JV17-6-2 representing the maximum value within this range. Europium anomalies are similar, ranging from 0.70 to 2.00, with most values around 0.80 - 1.10 and JV17-6-2 falling within this range as well at 0.93 (Table 2).

When normalized to JV17-6-2, the samples show a dominant trend of slight LREE enrichment (La – Eu), MREE depletion (Eu – Ho), and HREE enrichment (Ho-

Lu), with a significant negative Tm anomaly due to the positive anomaly seen in the chondrite normalized amygdale sample (Figure 20). Once again, LREE appear to have experienced a sudden overall decrease with increasing distance from the host rock in JV17-1a, but no other deviations are immediately apparent apart from those mentioned earlier.

Table 2. Minor and REE concentrations for calcite veins and amygdales.

Sample	Mn^{2+} (ppm)	Fe^{2+} (ppm)	ΣREE (ppm)	ΣLa-Gd (ppm)	ΣTb-Lu (ppm)	Ce/Ce*	Eu/Eu*	ΣLREE/ ΣHREE
JV17-1a-2	3780	532	1687.40	1687.40	54.40	0.87	0.80	31.02
JV17-1a-3	3360	525	592.20	592.20	33.94	1.10	0.93	17.45
JV17-1a-4	2240	494	342.35	342.35	27.19	0.96	0.92	12.59
JV17-1a-5	712	382	4.02	4.02	0.23	0.79	1.69	17.77
JV17-1a-7	1769	416	39.02	39.02	4.45	0.95	0.87	8.77
JV17-1a-8	3312	846	29.81	29.81	7.27	0.76	1.16	4.10
JV17-1a-9	1813	447	30.69	30.69	3.94	0.98	1.93	7.78
JV17-1a-10	2600	428	642.29	642.29	17.27	1.02	0.89	37.18
JV17-1a-11	1670	373	383.57	383.57	10.38	0.96	0.90	36.97
JV17-1a-12	4230	632	722.36	722.36	24.66	1.04	0.98	29.29
JV17-2-1	5250	600	355.39	335.99	19.40	**1.18**	0.93	17.32
JV17-2-2	5940	481	68.53	58.97	9.56	1.09	0.90	6.17
JV17-2-3	1996	473	23.83	20.73	3.10	0.95	1.13	6.68
JV17-2-4	2660	382	99.11	94.93	4.18	0.81	1.69	22.74
JV17-2-5	6290	578	89.14	82.51	6.63	0.89	1.01	12.44
JV17-2-6	4400	518	257.71	248.51	9.20	1.06	1.03	27.03
JV17-2-7	5510	687	375.71	353.43	22.28	1.01	0.95	15.87
JV17-6-2	**718**	**347**	**1.00**	**0.97**	**0.03**	**1.17**	**0.93**	**28.87**
JV17-9-1	7160	719	768.72	753.62	15.10	0.81	0.70	49.91
JV17-9-2	9380	1320	746.16	731.82	14.34	0.88	0.78	51.04
JV17-9-3	7070	1138	248.09	243.57	4.52	0.95	0.73	53.92
JV17-10-1	6150	675	174.61	171.92	2.69	0.93	0.81	63.99
JV17-10-2	2258	417	157.35	153.75	3.60	1.01	0.77	42.71
JV17-10-3	12090	9630	96.76	94.82	1.94	0.78	0.78	48.77
JV17-10-4	4123	1563	61.42	59.02	2.40	0.79	0.72	24.58
JV17-10-5	5473	1087	28.17	26.57	1.60	0.81	0.73	16.64
JV17-10-6	4025	1445	79.81	76.96	2.85	0.80	0.71	27.04
JV17-11-1	5892	980	133.09	130.93	2.17	0.92	1.75	60.46
JV17-11-2	3828	447	59.24	58.17	1.07	0.86	1.33	54.34
JV17-11-3	7001	5110	158.59	150.90	7.68	0.90	0.89	19.65
JV17-12-1	1780	553	71.02	69.49	1.53	0.94	2.00	45.46
JV17-12-2	1800	510	53.14	50.83	2.31	0.85	1.52	22.00
JV17-12-3	5070	800	280.44	270.16	10.28	0.77	0.87	26.29
JV17-12-4	3036	509	217.47	208.55	8.92	0.85	1.02	23.39
JV17-12-5	5390	665	238.68	223.70	14.98	0.98	0.87	14.93
JV17-12-6	4720	670	191.11	183.99	7.12	0.98	0.99	25.83

Note: Bolded values are sample JV17-6-2, used in Figure 20 to normalize REE data for comparison with a bedrock fluid source.

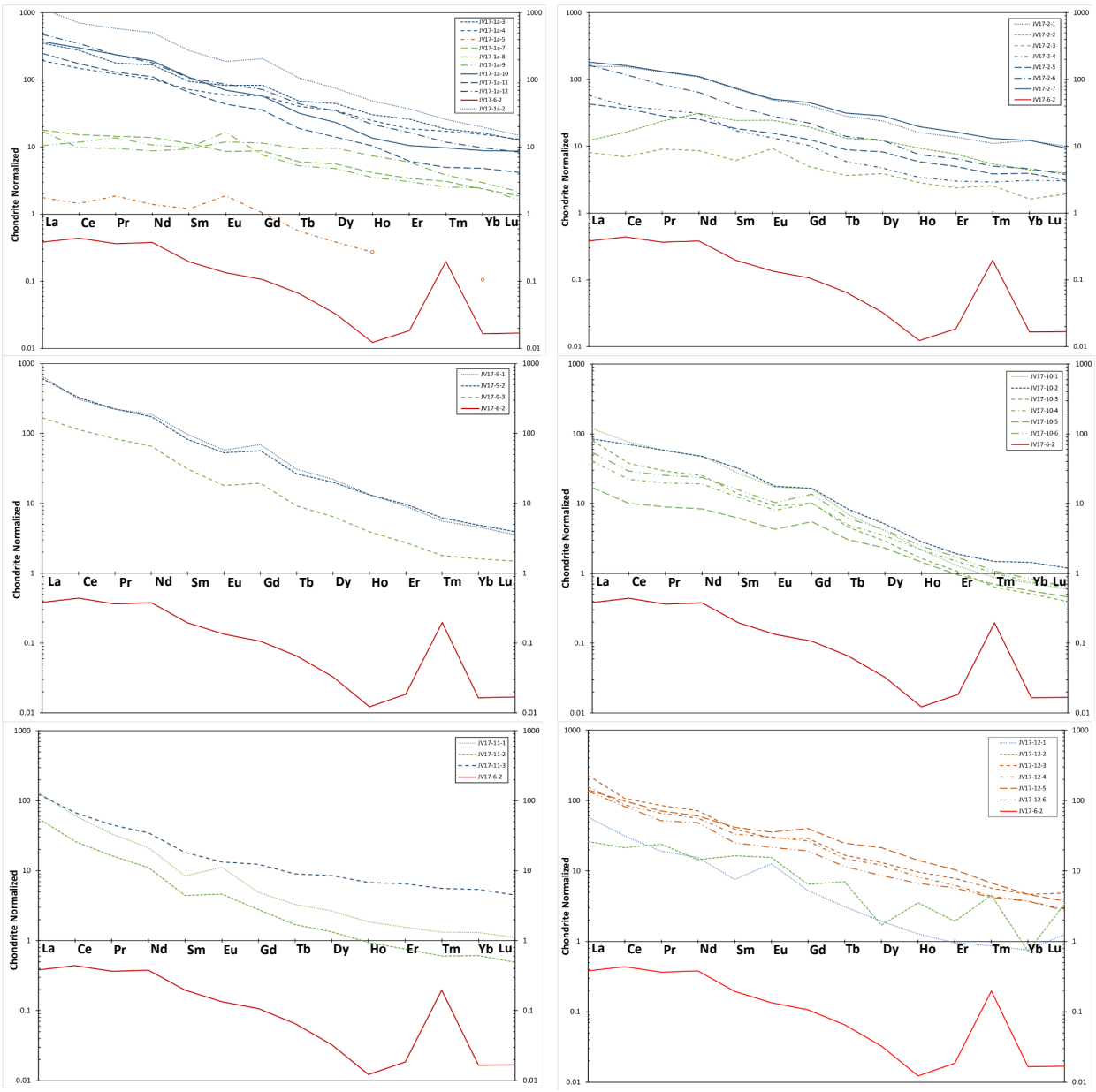

Figure 19. REE plots for Samples JV17-1a (top left), JV17-2(top right), JV17-9 (middle left), JV17-10 (middle right), JV17-11 (bottom left), and JV17-12 (bottom right) with comparison to amygdale JV17-6 (solid black line). Missing analyses capped off in JV17-1a-5. Note the high Th anomaly within amygdale JV17-6-2 (Uysal et al. 2007 for more). For corresponding laser-spot locations, see Figures 5-10.

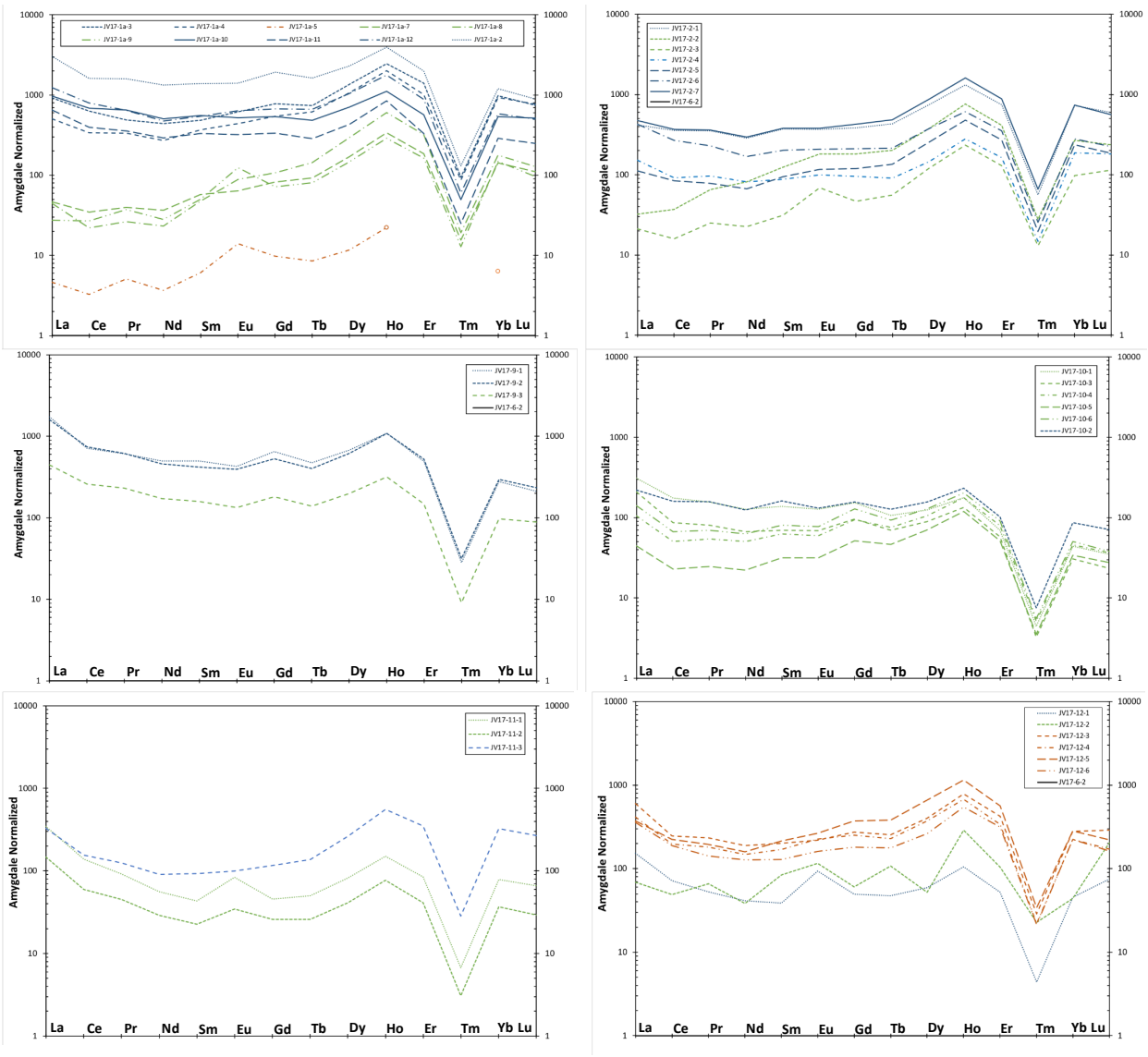

Figure 20. REE plots for Samples JV17-1a (top left) JV17-2(top right), JV17-9 (middle left), JV17-10 (middle right), JV17-11 (bottom left), and JV17-12 (bottom right) normalized to amygdale JV17-6-2. For corresponding laser-spot locations, see Figures 5-10.

4.4 Stable Isotope Analyses

Thirty-nine carbon and oxygen stable isotope analyses were collected within this study. Values for $\delta^{13}C_{VPDB}$ in vein samples ranged from -1.90‰ to –9.87‰, while $\delta^{18}O_{VPDB}$ values ranged between -11.83‰ and -1.86‰ (Table 3). All $\delta^{13}C$ errors were <0.1‰, while $\delta^{18}O$ errors were <0.15‰, based on the standard deviation of three replicate analyses per sample (excluding sample JV17-10-6). It should be noted that both the maximum and minimum $\delta^{18}O$ values for this range were found within vein

sample JV17-1a, as analyses immediately adjacent to each other and nearest to the host rock. Across individual veins, the carbon isotopes revealed <3.0‰ variation, except for JV17-11, where >3.0‰ was observed between two separate, crosscutting veins (Figure 10). In contrast, $\delta^{18}O$ varied by >3‰ for at least one pair of adjacent analyses in all veins except for JV17-11 and 12, with maximum variation ~10‰ within JV17-1a. However, for most analyses (apart from JV17-1a), variation was <2‰. Variations in $\delta^{13}C$ and $\delta^{18}O$ are only weakly correlated, while no systematic fractionation trends (i.e. consistent changes, linear or otherwise) were observed within any veins that would clearly fit observed growth trends.

While JV17-6 was too small to collect sufficient powder for analyses, studies across Amygdale JV17-10 show little variation in either $\delta^{13}C$, ranging from -3.15‰ to -4.09‰ or $\delta^{18}O$, ranging from -9.75‰ to -5.24‰ (Table 2). One outlier occurs distinct from these values; JV17-10-6 has an anomalously lower $\delta^{13}C$ value of -6.44‰, but a slightly higher $\delta^{18}O$ value of -5.24‰. Analytical notes suggested relatively low peaks, perhaps due to the presence of a non-calcite material (A. Pye, unpublished). However, minor element analyses for this region of the sample confirm that calcite is present, and the corresponding $\Delta47$ – stable isotope analysis gives relatively similar $\delta^{13}C$ or $\delta^{18}O$ values. Therefore, these results cannot be excluded to give a more unified amygdale value for $\delta^{13}C$ or $\delta^{18}O$.

Table 3. $\delta^{13}C$ and $\delta^{18}O$ stable isotope values for Lunan Bay calcites (‰).

Sample	$\delta^{13}C_{VPDB}$	1 Std. Dev.	$\delta^{18}O_{VPDB}$	1 Std. Dev.	$\delta^{18}O_{VSMOW}$
JV17-1a-1	-3.80	0.02	-1.36	0.03	28.61
JV17-1a-1C	-3.94	0.01	-7.13	<0.01	22.66
JV17-1a-2	-3.26	0.02	-11.83	0.03	17.81
JV17-1a-3	-3.50	0.02	-4.36	0.03	25.51
JV17-1a-4	-1.90	0.02	-7.67	0.03	22.11
JV17-1a-5	-3.36	0.02	-5.64	0.03	24.20
JV17-1a-6	-3.05	0.02	-6.80	0.03	23.00
JV17-1a-2C	-3.99	<0.01	-8.81	<0.01	20.93
JV17-1a-7	-3.86	0.02	-10.71	0.03	18.96
JV17-1a-8	-2.41	0.02	-5.11	0.03	24.74
JV17-1a-9	-3.04	0.02	-10.10	0.03	19.59
JV17-1a-10	-2.84	0.02	-7.29	0.03	22.50
JV17-1a-11	-5.21	0.02	-8.29	0.03	21.46
JV17-2-1	-3.66	0.02	-6.89	0.03	22.91
JV17-2-2	-4.47	0.02	-10.97	0.03	18.70
JV17-2-3	-4.51	0.02	-9.74	0.03	19.97
JV17-2-4	-4.22	0.02	-11.43	0.03	18.22
JV17-2-5	-4.55	0.02	-10.09	0.03	19.61
JV17-2-1C	-4.18	<0.01	-11.89	<0.01	17.75
JV17-2-6	-3.70	0.02	-11.46	0.03	18.19
JV17-2-7	-3.46	0.02	-12.10	0.03	17.53
JV17-2-8	-3.51	0.02	-11.13	0.03	18.53
JV17-9-1	-3.55	0.05	-9.51	0.05	20.21
JV17-9-2	-3.08	0.02	-9.34	0.09	20.38
JV17-9-3	-3.39	0.05	-8.25	0.06	21.50
JV17-10-1	-3.43	0.02	-7.75	0.05	22.02
JV17-10-2	-4.04	0.02	-9.08	0.06	20.65
JV17-10-3	-4.08	0.05	-7.98	0.08	21.78
JV17-10-4	-4.09	0.04	-9.75	0.03	19.96
JV17-10-5	-3.15	0.07	-6.19	0.14	23.63
JV17-10-6*	-6.44	0.11	-5.24	0.18	24.61
JV17-10-1C	-5.54	<0.01	-8.58	<0.01	21.16
JV17-11-1	-6.15	0.03	-10.77	0.06	18.91
JV17-11-2	-9.87	0.05	-12.89	0.10	16.72
JV17-11-3	-5.64	0.04	-12.78	0.06	16.83
JV17-12-1	-3.35	0.04	-12.23	0.04	17.40
JV17-12-1C	-3.04	<0.01	-13.15	<0.01	16.45
JV17-12-2	-3.27	0.05	-12.80	0.11	16.81
JV17-12-3	-3.19	0.06	-12.18	0.09	17.45
JV17-12-4	-3.33	0.05	-13.21	0.07	16.39

4.5 U-Pb Dating

Three samples were dated using U-Pb calcite geochronology; JV17-1a, JV17-2, and JV17-5 (not used otherwise within this study but consisting of a large mass of highly stained cockscomb calcite collected from what appeared to be a fault zone). Of the three samples dated, JV17-2 gave the most precise age of 328 ± 27 Ma, while JV17-1a gave a less precise age of 381 ± 95 Ma. Both samples show mean squared weighted deviation (MSWD) values outside of the expected range for a single population (>1, with JV17-1a being >>1 at 8.6), with scatter in these cases consistent with variable common Pb isotope composition (higher variations up to 100 ppm in JV17-1a versus ~ 2 ppm in JV17-2. This scatter is taken into account in the age uncertainties, but absolute ages should be viewed with caution as a result (Roberts et al. 2016). However, given that JV17-2 falls within the error of JV17-2, and that multiple phases of growth are observed within JV17-1a, both values are probably still applicable to this study. For comparison, sample JV17-5 gives an age of 310.3±7.2, supporting the validity of the previous two analyses despite strong deviation from a single population (MSWD – 16). Furthermore, maximum U contents range from 429 ppb in JV17-1a, to 683 ppb in JV17-2, enough for age dating to be relatively successful (Roberts et al. 2016).

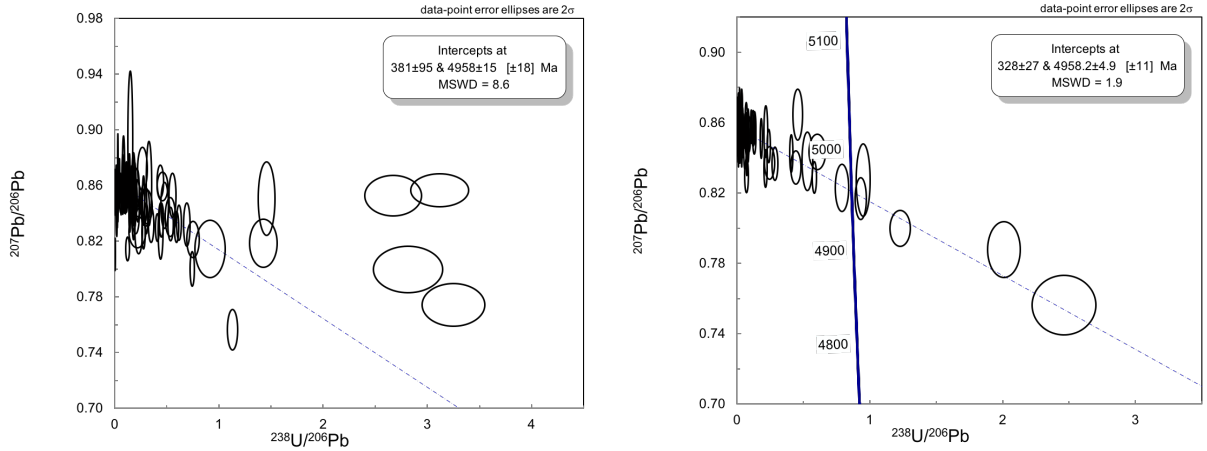

Figure 21. Tera-Wasserburg concordia plots showing 238U/206Pb versus 207Pb/206Pb. Left: JV17-1a. Right: JV17-2. MSWD—mean squared weighted deviates. Age regression visible as dashed blue line, Tera-Wasserburg Concordia line as dark blue line.

4.6 Clumped Isotope (Δ_{47}) Paleothermometry

A subset of five drill locations covering four samples were selected for Δ_{47} analysis; these values are highlighted in Table 4. The Δ_{47} values range from 0.426‰ to 0.599‰, with deviations less than ±0.03‰ based on three analytical runs per sample. These values correspond to calcite precipitation temperatures of ~185 °C to ~68 °C, respectively, with average temperature errors ranging between ~30 °C for the former and < 5 °C for the latter. Two analyses of JV17-1a led to relatively similar temperatures near bedrock and within the matrix of ~120 °C, although the latter measurement appears to be more precise based upon temperature deviation. Potential bond-reordering was assessed (J. MacDonald, unpublished), using ambient temperatures derived from a 30 °C/km geotherm and the burial model of Marshall et al. (1994), and was determined to have no effect on the samples presented here (MacDonald et al. 2017). This suggests that (assuming that the bedrock model is correct) the temperatures represented here are original temperatures of formation, and that bond-reordering had little effect on altering perceived temperature calculations (Appendix 1). Furthermore, given the large amount of powder required to perform these analyses, it was impossible to ensure that all powder came from a single calcite crystal. This is likely the reason for the 'averaging' seen in the $\delta^{18}O$ and $\delta^{13}C$ values with relation to those values determined from adjacent drill locations (Figure 6-11).

Using the clumped isotope temperature determinations (assuming an initial precipitation temperature), the $\delta^{18}O$ of the source fluid were determined (after Kim & O'Neil 1997) (Table 4). Vein samples generally exhibit $\delta^{18}O$ values nearing 10‰, while the amygdale JV17-10 has a much lower value of ~1‰.

Table 4. Clumped isotope (Δ_{47}) values and temperature determinations (after Kelson et al. 2017) with corresponding back-calculated $\delta^{18}O$ source fluid values (after Kim & O'Neil 1997) for vein and amygdale calcites from Lunan Bay, Scotland.

Sample	Δ_{47} Average ± 1 Std. Dev. (‰)	Temperature Average ± 1 Std. Dev. (°C)	$\delta^{18}O$ Source fluid ± 1 Std. Er. ($‰_{VSMOW}$)
JV17-1a-1C	0.489 ± 0.029	118 ± 22.7	9.6 ± 3.4
JV17-1a-2C	0.478 ± 0.013	125 ± 11.4	8.7 ± 1.6
JV17-2-1C	0.426 ± 0.013	181 ± 16.5	11.2 ± 1.8
JV17-10-1C	0.599 ± 0.004	68 ± 2.41	1.4 ± 0.5
JV17-12-1C	0.421 ± 0.021	189 ± 29.4	10.6 ± 3.2

- Chapter 5: DISCUSSION -

5.1 Textures & Growth Mechanisms

Calcite crystal morphology and crosscutting relationships observed within optical and cathodoluminescent studies can used to make inferences into the mode of fracture propagation and vein growth limitations (Bons et al. 2012, McNamara et al. 2016). For example, syntaxial growth would suggest progressive mineralization in the direction of least stress during fracture propagation, while anhedral-euhedral calcite growth would be suggestive of crystal growth within a free medium, i.e. without any preferential growth directions due to stress orientation or fracture opening (Bons et al. 2012; Ramsay et al. 1980). The presence of suture lines, often vuggy in texture and containing rich Fe^{2+}/Mn^{2+} oxide concentrations, would suggest a termination in growth where these species were last to precipitate, therefore inferring a relative growth direction and constraining fluid flow during the last stages of precipitation (Barker et al. 2006; Maskenskaya et al. 2015). Within most samples (JV17-2, JV17-9, JV17-12), there is a simple progression from syntaxial bedrock growth into euhedral central growth, suggesting a single crack-seal event. However, within multiple samples (JV17-1a in particular) crosscutting species found more central to the vein may be suggestive of a secondary/ alteration growth phase, a change in stress regimes during fracture propagation, or if minor element fluctuations are any guide, a change in fluid chemistry (see 4.1 for more on this) (Bons et al. 2012; Maskenskaya 2015). Sample JV17-11 also records a change in vein growth, with a transition to stretched or fibrous crystals growth after initial syntaxial bladed growth. These complex growth histories would suggest either a sudden change in deformation rate or multiple crack sealing events, although given the optical extinction of the crystals, the former is more likely (Ramsay et al. 1980; Bons et al. 2012). Furthermore JV17-11 also shows clear evidence of a Fe^{2+}-oxide rich vein crosscutting a stretched vein (different in form than the suture lines discussed earlier) suggesting multiple discrete deformation events with potentially different source-fluids or degrees of bedrock interaction.

This study used CL to qualitatively determine chemical heterogeneity across multiple calcite veins, which may suggest evolution of minor element concentrations within the precipitating fluids. However, no clear patterns were observed that would

suggest different fluid sources, or a systematic variation with distance from the bedrock during syntaxial growth (unlike in similar studies by Denniston 1997 or Sturrock et al. 2017). At high concentrations (>800 ppm), Mn^{2+} does not behave linearly with regards to CL signature, but may engage in 'self-quenching', resulting in less cathodoluminescent calcites (Maskenskeya 2015). The concentrations of Mn^{2+} found here are, on average, five times larger (~4200 ppm) than this, suggesting that a strong self-quenching effect is likely obscuring visible recognition of chemical zonation from CL data (Machel 1985; Maskenskaya 2015). Zonation observed along growth boundaries as well as along cracks/ surface fractures is likely due more to changes or defects in the crystal lattice, or preferential Ca^{2+} replacement with Mn^{2+} over Fe^{2+} at certain sites during the growth of the crystal, instead of changes in source fluid chemistry (Machel 1985; McNamara et al. 2016). These findings suggest that CL may not be the best way to determine changes in fluid/ crystal chemical composition where high concentrations of Mn^{2+} are present (e.g. within intermediate- mafic bedrock-hosted calcite deposits similar to those studies here). As a result, this study places constraints on previous studies (e.g. Blyth et al. 2004) that interpreted homogenous stable isotope composition based on uniform CL signatures. However, data collection during this study was collected at intervals of 10^3 to 10^4 μm in between analyses, while changes in minor and trace elements are known fluctuate highly over ~10^2 μm (Barker et al. 2006). This may suggest that fluid chemistry is still having an effect on small scale calcite zonation, and is just being lost due to the spatial accuracy of the analyses presented here.

5.2 Temperature & Timing of Calcite Precipitation

The two samples dated using LA-ICPMS U-Pb calcite geochronology gave ages of 381 ± 95 Ma (JV17-1a) and 328 ± 27 Ma (JV17-2). These ages are within error of each other, and generally cover the range of time between deposition of the MVF, through to maximum burial (Figure 21) (Marshall et al. 1994). The 385 Ma absolute age corresponds to the initial burial of 2.6 km, while the 328 Ma age corresponds well to a slight change in burial rate reflected by vitrinite reflectance studies (Marshall et al. 1994).

Three Δ_{47} temperatures are also noted: ~185 °C, ~120 °C, and ~70 °C. The Δ_{47} temperature increase with increased geothermal temperature (assuming a 30 °C/km

continental geotherm derived from the burial model and given the proposed U-Pb ages), but do not appear to have precipitated at equilibrium with the ambient temperature of the bedrock (Figure 22). While amygdale sample JV17-10 fits relatively well with the proposed burial assuming a pre-vein deposition suggested by various amygdale-vein crosscutting relationships, the burial model requires higher ambient temperatures (between 50-90 ^{o}C ambient temperature increase) in order to fit the suggested Δ_{47} vein temperature calculations. (Figure 22). Therefore, these uncertainties would suggest either inaccurate ages of formation (given that bond re-ordering has been accounted for), an inaccurate geotherm estimate, an inaccurate burial model stratigraphy, or hot fluid precipitating within a cooler host rock.

Inaccurate age determinations are unlikely (taking into account age uncertainties) given that ambient temperatures fail to increase enough to fit the higher Δ_{47} precipitation temperatures for any period of regional burial history. A hotter geotherm is also unlikely, given that the 30 ^{o}C/km assumed geotherm is already at the upper limit of normal continental geotherms, even along active tectonic fronts. However, an inaccurate burial model is possible, given some of the assumptions used during its creation. Marshall et al. assumed reduced stratigraphic thicknesses for the Arbuthnott-Garvock and Strathmore groups in order to fit the vitrinite reflectance values to those measured within the Arbuthnott (1994). This was justified within the original study due to noted inaccuracies with previous stratigraphic thickness calculations based on dip measurements and trigonometry as opposed to direct logging. Therefore, it is possible that the stratigraphic thickness of the Arbuthnott-Garvock and Strathmore groups, as well as overlying (poorly preserved) Carboniferous sequences have been underestimated, resulting in deeper MVF burial estimates being unaccounted for. However, to fit the Δ_{47} temperatures to the burial model would require additional burial of the MVF between 1.5 (JV17-1a)- 4 km (JV17-2, JV17-12) suggesting that the Arbuthnott-Garvock (~3 km) and Strathmore thickness estimates have been underestimated by 50-150 % within the first 50 Ma of depositional history, which is highly unlikely even given the assumptions noted above (Hole et al. 2013). Therefore, burial depth uncertainties are unlikely to explain the discrepancy between Δ_{47} and burial model ambient temperatures determinations at the given U-Pb age determinations.

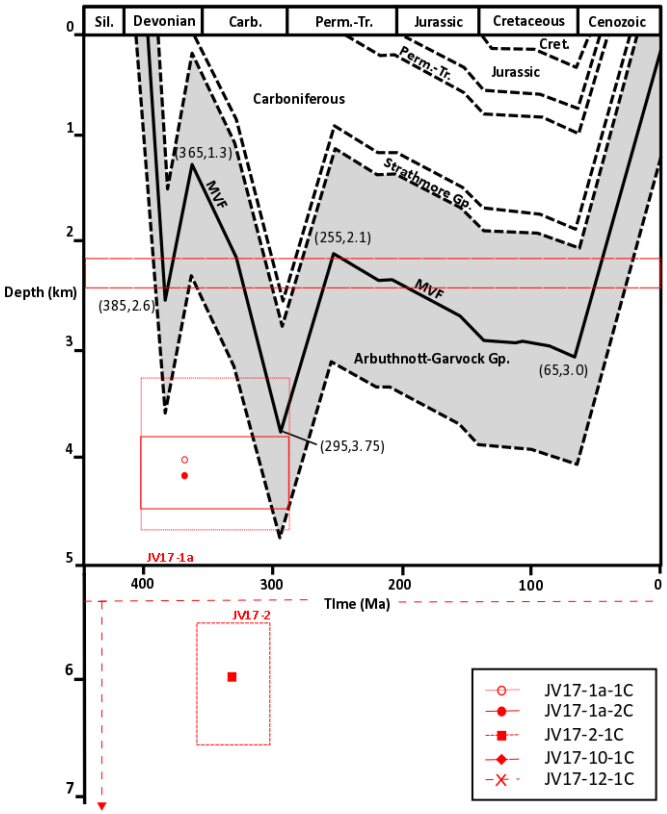

Figure 22. Burial history for the lower ORS and Arbuthnott-Garvock group (gray) from the Forfar area with the MVF and corresponding values (age, depth) included, after Marshall et al. 1994. Included are samples within this study, with age-depth boxes bounded by uncertainty in U-Pb dating and clumped isotope temperature calculations, with depth calculated from temperature based upon a continental geotherm of 30 °C/km.

Assuming that the Δ_{47} temperature calculations represent the original precipitation temperature (i.e. that no bond reordering has taken place, as is shown in Appendix 1), the $\delta^{18}O$ of the source fluid can be used to help explain the lack of similarity between ambient and precipitation temperature. Vein samples presented here generally have $\delta^{18}O$ fluid values nearing 10‰$_{VSMOW}$, similar to those seen from magmatic (5.7 ± 0.3‰ to ~10‰) and metamorphic fluids (~5‰ to ~25‰), as well as andesitic and rhyolitic melts (Lu et al. 2017; Rollinson 1993; Ryb et al. 2017) (Figure 23). Meanwhile, amygdale JV17-10 fell exhibits source fluid values nearer to 1‰, similar to estimated values for meteoric (sea) waters but removed from expected values for fluids precipitated from basalt (Rollinson 1993; Ryb et al. 2017). It is possible in this case (as will be discussed in Sections 5.3 and 5.4) that this amygdule experienced mixing of two fluids with different chemistries (as is suggested in Lu et al. 2017). Therefore, the most likely cause of this low amygdale value is the downward percolation of meteoric waters at shallower depths, given the large amount of fluvial deposition coeval with MVF formation, and the relative porosity expected from newly deposited lavas (Lu et al. 2017; Morad et al. 2010) (see section 5.4 for the

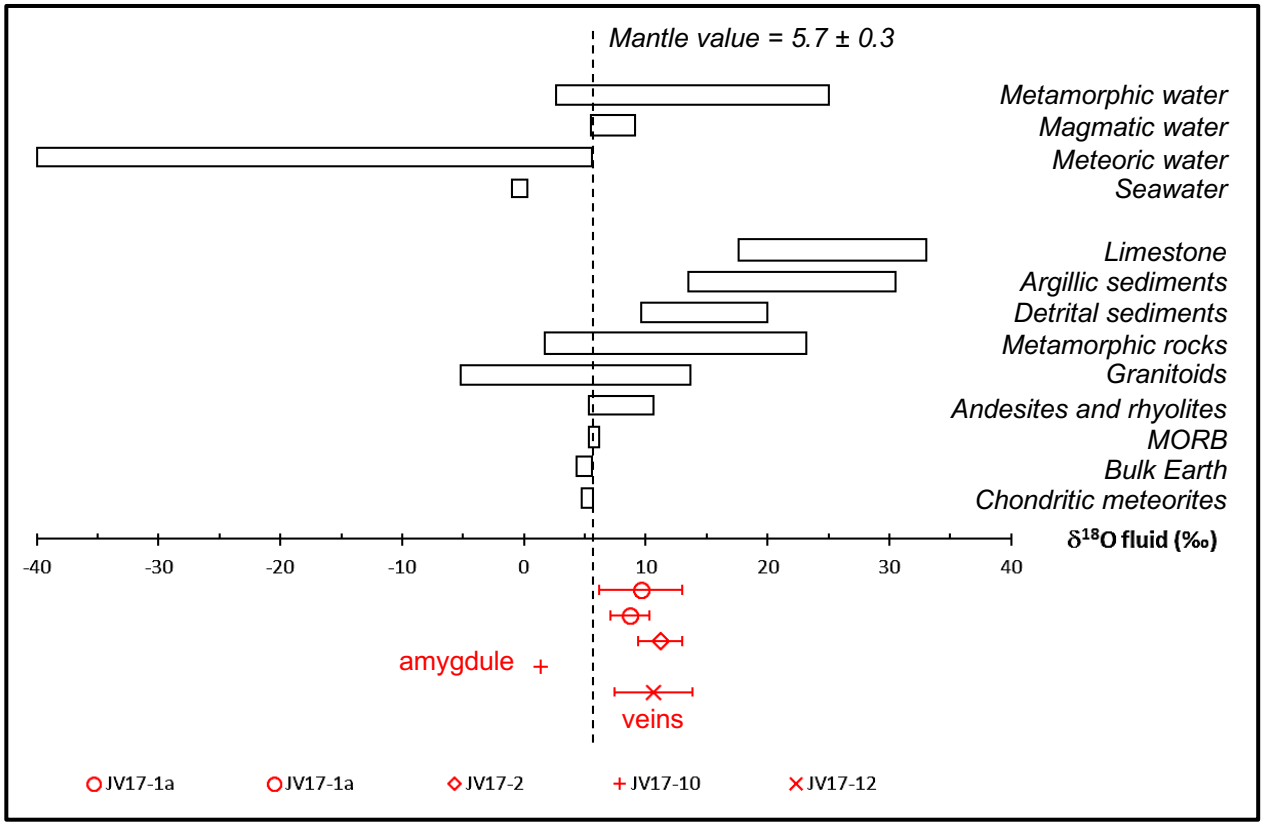

Figure 23. Natural oxygen isotope reservoir δ ^{18}O fluid values (‰$_{VSMOW}$) with clumped-isotope derived compositions for samples from within this study (after Rollinson et al. 1993 and references contained within).

geological implication derived from these findings). Therefore, the most likely reasoning behind the elevated Δ_{47} vein precipitation temperatures is disequilibrium with the bedrock ambient temperature and the heated, depth-sourced magmatic/ metamorphic fluids during precipitation.

5.3 Bedrock Interaction & Fluid Source

5.3.1 Minor & Trace Element Interpretations

Previous studies have suggested that minor and trace element zoning patterns across calcite veins can be used to help constrain petrogenesis, where cooler meteoric waters percolating down through open fractures are less likely to react with the country rock than upward-flowing hot magmatic/hydrothermal fluids, and where fluctuating/ oscillatory behaviour may therefore be suggestive of either a change in fluid chemistry (Barker and Cox 2011) or fluid mixing (Bons et al. 2012; Wogelius 1997). Unfortunately, many of these studies lack definitive precipitation temperatures and fluid sources,

limiting any interpretations of bedrock-fluid interaction or petrogenetic determinations. The findings of Section 5.2 may be able to overcome some of these limitations.

Within this study, higher concentrations of minor elements are generally found in minor veins versus major veins. As would be expected by the fluid-bedrock ratio, these higher Fe^{2+} and Mn^{2+} concentrations would suggest that fluids flowing through constrained fluid pathways experience higher degrees of bedrock buffering in comparison to those flowing through larger, less constrained fluid pathways (Wogelius et al. 1997). This is supported by observations of single phase growth within these minor veins in comparison to the more complex, multiple phase growth observed within some of the major veins. Furthermore, this may explain the fluctuations in minor element concentration across the vein, given the ability for larger fluid circulation and therefore more interaction with multiple fluid sources or variations in fluid chemistry. However, these fluctuations appear to be uncorrelated with the direction and breaks in growth. Given that minor and trace element concentrations are known to fluctuate widely with growth direction (often an order of magnitude over only a few hundred μm) it is ultimately difficult to determine fluid source chemistry as a function of growth (Barker et al. 2006; Barker & Cox 2011; Maskenskaya 2015; Möller et al. 1991).

There are distinct Δ_{47} temperature difference present within vein samples JV17-1a, JV17-2, JV17-12, and amygdale JV17-10, yet these temperatures do not correlate within increased concentrations of Mn^{2+} or Fe^{2+} (Figures 12, 13, 15, and 18). Therefore, while there is significant scavenging of these minor elements within all veins, the temperature of the fluid is unlikely to have a significant effect (as previously suggested). Instead, the fluid-bedrock ratio/ bedrock surface available appears more likely to have an effect on enhanced minor and trace elements scavenging from the bedrock, as is suggested by Barker et al. (2006) and others (Barker et al. 2011).

5.3.2 REE Interpretations

Where efforts to determine source fluid-chemistry based on minor element concentrations have failed, Lee et al. (2003) demonstrated that REE can provide evidence of the solution chemistry involved in the precipitation of calcite veins. While relatively insoluble within low temperature metamorphic and hydrothermal systems REE behave as a coherent group in natural environments due to their similar ionic potential

and oxidation state and are therefore often used as petrogenetic indicators of fluid source in hydrothermal fluids (Barker et al. 2006; Maskenskaya et al. 2015; Rollinson et al. 1993; Sturrock et al. 2017). With this known, REE data can be interpreted two different ways: by concentration (ΣREE) and fractionation trend (ΣLREE/ΣHREE). The former is slightly more ambiguous, as it is subject to a multitude of external conditions that are difficult to quantify within studies of this nature. These include changes in crystal morphology (Barker & Cox 2011), preferential HREE complexing with CO_3^{2-} and OH^- anions (Barker et al. 2006), precipitation temperature dependence (Maskenskaya 2013), LREE remobilization during post-formation alteration events (Bau & Möller 1992), and unknown bedrock sources. In contrast, REE fractionation is relatively constant across all forms of calcite, largely independent of crystal morphology and temperature effects below 250 ^oC. REE fractionation trends can therefore give an insight into changing fluid source, although preferential LREE inclusion and remobilization still need to be considered (Bau & Möller 1992).

Within this study, concentrations of REE are generally magnitudes higher than those found in rivers and seawater (Rollinson 1993) and other studies with sedimentary derived fluids (Morad et al. 2010), with the exception of the amygdale standard JV17-6-2. This would suggest that the majority of the veins, as well as amygdale JV17-10, experienced significant fluid sourcing from an igneous source, while the amygdale standard experienced much less.

Within all samples chondrite normalization generally show heavy LREE enrichment, with decreasing enrichment through the HREE. This is expected in calcites, which should preferentially include LREE over HREE due to the smaller difference between the ionic radii of LREE and Ca^{2+} (Denniston 1997; Morad 2010). However, there are other differences that have an effect on the changes in LREE versus HREE fractionation. Within basaltic and andesitic rocks, preferential fractionation of LREE is common, primarily controlled by olivine, orthopyroxene, clinopyroxene, and hornblende. The partition coefficient of Lu, is a magnitude greater than for La, in basaltic liquids, albeit all REE are incompatible within these same rocks, and are therefore easily scavenged (Rollinson 1993). This would result in LREE-dominant REE enrichment in the fluid interacting with the bedrock and result in high LREE fractionation within the

calcite precipitate, as chemical sediments usually reflect the composition of the fluids they precipitate from (Rollinson 1993).

With this in mind, multiple fluid chemistries/ changes in bedrock-fluid interaction can be inferred from Figure 19. Sample JV17-1a appears to have four distinct fluids (defined by trend and concentration – divided into colours in Figure 19), suggesting a complex sealing process with progressive depletion of a long-term fluid where bedrock-inward crystal growth would progressively limit the amount of fluid-bedrock interaction, resulting in decreased REE scavenging and precipitation (see Barker 2006; Maskenskaya 2015 for similar findings). There are also slight differences between the two crosscutting veins in JV17-11 due to a more iron rich vein likely sourced from a different fluid chemistry, resulting in a slightly more enriched HREE signature. Meanwhile, relatively similar REE fractionation within JV17-9, JV17-10, and JV17-12 would suggest a single fluid source, although slightly different REE concentrations may once again be the result of fluid depletion with time. Taking the above uncertainties into consideration, it is likely that these veins (with the exception of outliers in JV17-1a and JV17-11) evolved from a similar fluid source.

Amygdale normalization (vein REE analyses/ JV17-6-2 REE analyses) can give further inferences into the degree of fluid-bedrock (MVF specific) buffering (Figure 20) (Rollinson 1993). With the large Tm anomaly accounted for earlier (also observed, yet not understood in Uysal et al. 2007, and with little literature on the subject) the dominant trend across most samples is that of LREE (La – Eu) depletion, MREE (Eu – Ho) enrichment, and HREE (Ho-Lu) depletion. This relatively constant trend suggests that that the primary bedrock-buffer to all crystallizing fluids was MVF basalt-andesites, where MREE depletion is commonly seen within early stage precipitation of fluids (when normalized to the source fluid, here assumed to be purely bedrock derived) (Barker & Cox 2011). However, different trends observed within samples JV17-1a and JV17-11 suggest that other minor fluid sources may also be present and may suggest a more complex fracture/growth history for these samples.

This normalization technique also reveals some unique differences in fluids that were not clearly discernable with chondrite-normalization. Analyses JV17-2-2 and JV17-2-3 appear to have crystallized from a slightly different source fluid with less enrichment

in LREE in comparison to MREE, similar to that of JV17-1a-7 - JV17-1a-9. Once again, bedrock surface access might be the cause of this depletion in LREE, where a lower bedrock-fluid ration would lead to less overall scavenging (Barker et al. 2006). Similar to variations in Fe^{2+} and Mn^{2+}, this normalization technique shows no correlation between precipitation temperature and changing REE trend/ scavenging. Therefore, these REE trends generally support the idea of a singular fluid source, or very strong degrees of bedrock-fluid buffering capable of disguising the original REE signature.

5.3.3 Ce & Eu Anomalies

Ce and Eu anomalies are indicative of changes in fluid oxidation and fluid chemistry, respectively, as they are less influenced by compositional zonation than other minor elements and REE given their non-trivalent elemental equivalents (Barker et al. 2006; Barker & Cox 2011). Ce occurs as both the Ce^{3+} and Ce^{4+} (depending on its oxidation state) and should follow the trends of its immediate neighbours (La and Pr) when normalized ($Ce/Ce^* = 1$, where Ce^{3+} is the primary species). However, negative Ce anomalies may result from oxidized fluids, where Ce^{4+} has a dominant presence (Denniston et al. 1997; Rollinson 1993). Therefore, Ce anomalies (especially with regards to amygdale normalization) can be indicative of increased oxidation of the fluid source, and potentially give evidence to changes in fluid source independent of the additional factors that complicate REE interpretation (Barker et al. 2006; Bau & Möller 1992). Within this study, most samples normalized to chondrite contain negative to neutral Ce anomalies, with the exception of analyses that occur closer to the bedrock in samples JV17-2, and JV17-6-2, which exhibit slightly positive anomalies (Table 3). This would suggest that (1) these crystal growths phases had higher degrees of bedrock interaction (were more highly oxidized), (2) bedrock interaction decreased with progressive vein growth, and (3) the fluid source was likely magmatic in origin, as positive Ce anomalies generally arise within chemical sediments precipitated from seawaters (Rollinson et al. 1993). However, this finding is not supported within minor veins, or within JV17-10, which would also be expected to exhibit positive Ce anomalies given (assumedly) significant bedrock interaction. This would suggest that there may be other controls on Ce fractionation, outside the scope of discussion within this study (see Barker et al. 2006 for more).

When normalized to amygdale JV17-6-2, Ce anomalies appear to be consistently <1. This would suggest that, while high MVF buffering is likely within most magmatically sourced fluids, either none of the fluids except the amygdale standard precipitated directly from a single bedrock-sourced fluid, or that the amygdale standard has a certain degree of seawater fluid-interaction effectively raising Ce concentrations (Barker et al. 2006; Denniston et al. 1997). While this places complications on using JV17-6-2 as a bedrock proxy, it may be useful when considering amygdale JV17-10 a stable isotope-bedrock proxy, as this sample has likely experienced a lower degree of meteoric fluid interaction despite the calculations of $\delta^{18}O$ fluid in section 5.2.

Within hydrothermally sourced carbonates, Eu anomalies are controlled by two factors: the Eu^{2+} content of the host rocks (Barker et al. 2006) with which fluids are interacting, and precipitation temperature (Bau & Möller 1992; Uysal et al. 2007). Host rock Eu content is primarily controlled by the presence (or absence) of Ca^{2+} rich-plagioclase, primarily in the form of anorthite, found within mafic igneous and volcanic rocks, although it is important to note that the MVF has little of this phase present (Barker et al. 2006; Thirwall 1982, 1983). At temperatures greater than 200-250 ^{o}C, Eu^{2+} begins to preferentially substitute for Ca^{2+} over the trivalent REEs, causing a positive Eu anomaly. Within this study, the majority of the Eu anomalies appear to be neutral or slightly <1, especially when normalized to the JV17-6-2, suggesting that there was generally little interaction with heavily enriched Ca-plagioclase rich bedrock, with fluid temperature also playing a minimal role in Eu fractionation. Some samples presented here contain Eu anomalies >1.5, and are not easily explained by REE trends, or Ce anomalies suggesting that bedrock/fluid buffering, or fluid mixing may be more complex, or that internal growth factors may be affecting Eu distribution (despite the findings of Barker et al. 2006).

5.3.4 C & O Stable Isotope Interpretations

Many geothermal studies use C and O isotopes alongside minor and trace REE analyses in order to interpret fluid source and bedrock buffering, where small variations (< 3‰$_{VPDB}$) of $\delta^{13}C$ and $\delta^{18}O$ are likely the result of bedrock buffering of the fluid

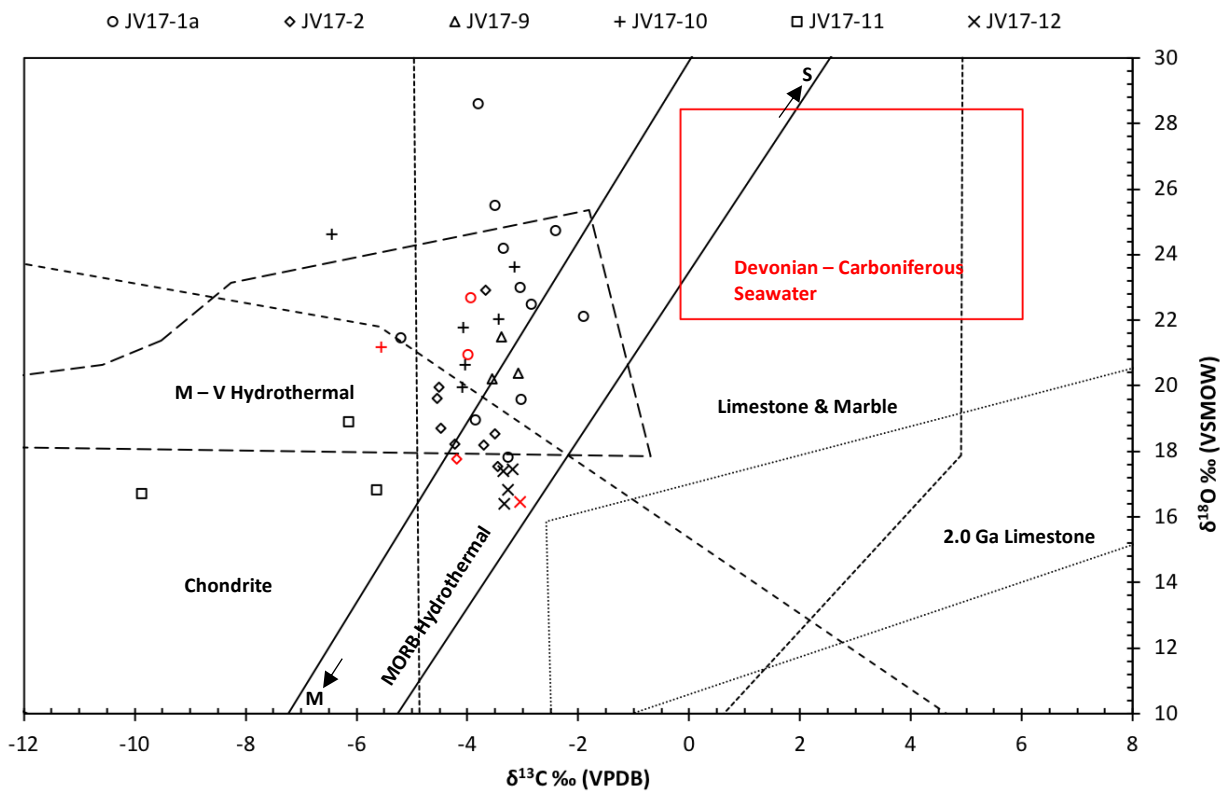

Figure 24. C and O stable isotope precipitates values analyzed within this study (red taken in conjunction with clumped isotope analysis) overlaying known carbonate precipitate reservoirs: Limestone and marble, Mid Ocean Ridge hydrothermal calcites (ranging from mantle (M) to seawater (S) derived), Mississippi Valley-type (M-V) hydrothermal calcites, chondrite, and $\pm 1\sigma$ range of seawater carbonates (Véizer et al. 1999) determined from Devonian-Carboniferous aragonite (red) (after Rollinson 1993, Figure 8.19, and references within).

(Hilgers & Sindern 2005) or stable temperature and chemistry (Barker et. al 2006; Lee et al. 1997), while large variations (>6‰$_{VPDB}$) may indicate mixing of distinct fluid types (Bons et al. 2012; Maskenskaya et al. 2015; Wogelius et al. 1997). However, the use of Δ_{47} temperature calculations to determine $\delta^{18}O$ source fluid fractionation make many of the assumptions taken in previous studies (Maskenskaya et al. 2015; Morad et al. 2017) unnecessary and can inform variations in $\delta^{13}C$ and $\delta^{18}O$ across individual veins as a result.

Within this study, vein and amygdale transects generally revealed <3.0‰ $\delta^{13}C$ variation, while $\delta^{18}O$ varied by >3‰ for at least one pair of adjacent analyses in most samples (although most variation was near to or <3‰). Assuming a relatively constant meteoric fluid source (as is supported by REE, Ce, and Eu interpretations), the results

of this study would suggest that the primary control on (the relatively stable) ^{13}C isotope fractionation was due to bedrock buffering of the fluid (Lee et al. 1997; Lu et al. 2017). Other studies have noted similarly negative $\delta^{13}C$ precipitate values, due to primary fluids likely evolving from a magmatic source as opposed to a meteoric one (Figure 24) (Lu et al. 2017). Meanwhile, fluctuation in $\delta^{18}O$ may be more indicative of infiltration of a distinct, seawater-derived fluid, albeit in very small quantities, as is common in many modern day geothermal systems (Lee et al. 1997; Lu et al. 2017). Similarly, the overall high $\delta^{18}O$ (SMOW) values (9.4–15.1‰) are suggestive of a magmatic source fluid. The $\delta^{18}O$ values of JV17-10 are also similar to those found within vein samples despite a lower source fluid value, suggesting that bedrock interaction must have occurred in significant quantities to alter the initially meteoric-magmatic mixed water derived $\delta^{18}O$ signature in addition to a primarily magmatic phase (Figure 24) (Lu et al. 2017).

5.4 Implications to the Geology & Tectonic History of the Region

The lines of evidence presented within this study also have implications towards the regional geology and tectonic history of the Lunan Bay area and wider MVT. First, vein growth morphology can give evidence of the stress regimes present during the timing of deposition (Bons et al. 2012). Observed absence of preferential vein orientation (within the field), a lack of significant shearing or beef vein growth, predominant euhedral crystal growth, and the presence of slight brecciated lithic fragments within single phases of crystal growth suggest decompression fracturing. This mode of fracturing, while containing fracture fill precipitatedwithin a period of larger scale compression/ sinistral strike slip transpression along the major terrane bounding faults (the Acadian Orogeny, along the Great Glen and Southern Upland Faults in the Late Silurian) likely occurred as a result of localized extensional/ uplift activity (Bons et al. 2012, Mendrum 2012; McNamara et al. 2016). This localized uplift could have been partially influenced by the back-arc volcanic activity occurring along the nearby Ayr-Ochil-Sidlaw anticline and Strathmore syncline (Figure 2) (Hole et al. 2013; Mendrum 2012; Rawley 2015). Furthermore, this activity was followed my minor transtension during the Mid-Devonian, potentially enhancing the the decompression-type of vein formation exhibited within this study. Therefore, while this regional compressional period is incompatible with significant uplift during the same time (assuming that the absolute

U-Pb ages presented here are accurate), they are not direct evidence against the findings of this study.

Knowing that the majority of the fluids precipitated from magmatic origins and their corresponding U-Pb ages, these findings can help to place constraints on the age of the MVF – something lacking in previous studies (Hole et al. 2013; Thirwall 1988). Previous studies have dated (via Rb-Sr dating techniques) the underlying Crawton Volcanic Group to 415.5 $\pm$ 5.8 Ma, using this value to infer an earliest age of deposition for the MVF (Thirwall 1988). This suggests that the MVF cannot be younger than the age of JV17-1a, 381 +/- 95 Ma, the oldest dated vein sample. While the uncertainty covers a period of deposition older than the date of deposition determined for the Crawton Group, the fact that this same vein contains an overwhelmingly magmatic $\delta^{18}O$ source fluid signature within a period of time where surficial processes were primarily fluvial dominated would suggest that the MVF was already at considerable depth during the time of vein deposition (Hole et al. 2013; Rawley 2015).

Finally, geological evidence suggests that volcanic activity for the region, including from the Montrose Volcanic Centre along the Ayr-Ochil-Sidlaw Anticline, took place over a period of 15 Ma during the Early Devonian (Figure 2) (Rawley 2015; Trewin & Thirlwall 2002). However, much of the younger cover rocks within the region have since been eroded away, obscuring any evidence of further Carboniferous (or younger) volcanic activity within the region, although significant evidence can be found in the southern Midland Valley around Edinburgh, UK. Knowing that the majority of vein calcites studied here evolved from magmatic/metamorphic origins, have ages ranging from the Mid Devonian to Mid Carboniferous, and precipitated out of equilibrium with the bedrock, the findings of this study would suggest that subsurface igneous activity within the region likely continued into the Carboniferous, coeval with the deposits preserved to the south (Figure 2).

5.5 Applications to Geothermal Energy

This study has a number of implications for geothermal energy, primarily with regards to underlying methodology. First, the sampling methods employed here prove to be a reliable, low cost way of accessing samples for analysis of fracture-filling processes as opposed to the coring techniques currently required in many active fields.

However, this study also places constraints on methodologies previously used to characterize fracture filling processes. While the use of optical petrology was successfully used here to quickly identify regions of growth and interest for further analyses, the use of CL as a zonation identification tool was put into question, especially in higher temperature, magmatic-derived fluids with high concentrations of excitatory minor elements (Mn^{2+}) (Blyth et al. 2004; Morad et al. 2010). Unlike previous studies, where interpretations of minor and trace REE analyses fluctuations were rather ambiguous due to a lack of known fluid source, this study has shown that Δ_{47}-derived $\delta^{18}O$ source fluid calculations can accurately constrain the effects of bedrock-interaction and fluid mixing suggested by these forms of analyses. Furthermore, this study highlights the potential use of REE trends normalized to a bedrock proxy to ascertain changes in fluid chemical composition, potentially addressing a common limitation in previous studies (Maskenskaya et al. 2013, 2015; Morad et al. 2010;). This technique, although applied here to fossil systems, could prove effective in modern carbonate/ basaltic geothermal systems where bedrock fluid proxies are easily observed, given the fine spatial resolution capacities of LA-ICPMS and EMPA analyses.

Most importantly, this study has shown (for the first time) the potential for combining LA-ICPMS calcite U-Pb dating and Δ_{47} temperature analyses has with regards to characterizing the thermal evolution of both fossil and active geothermal systems. However, it is important to note that there are potential errors with combining these methodologies that need to be accounted for, including bond reordering that may cause anomalously high temperature estimates and result in misinterpretations of fluid source, and bedrock fluid interaction. Furthermore, spatial resolution using Δ_{47} is still relatively poor, and this method will benefit significantly from increased measurement accuracy (i.e. less required sample material), especially where high special resolution is required (e.g. when studying the effects of individual well-bore scaling events).

- Chapter 6: CONCLUSIONS -

This study used a variety of techniques to understand the mode, history, and timing of fracture-filling within a fossil geothermal system from Lunan Bay, Scotland. The major findings of this study are:

(1) Primarily syntaxial, bedrock-outward crystal growth (Section 5.1) suggestive of progressive mineralization with fracture propagation, being replaced with euhedral growth suggestive of a period of free flow within the vein post fracturing, and representative of an uplifting stress regime (although not correlating with compressional tectonic activity resulting from the Acadian orogeny during the same time period) (Section 5.5).

(2) U-Pb calcite vein ages between ~380 and ~310 Ma, roughly corresponding to key events proposed within burial models for the region, which provide a youngest age limit of less that 410 Ma for the MVF lavas when combined with knowledge of a magmatic source fluid (Section 5.4).

(3) Clumped isotope temperature determinations, between 120 and 190 ^{o}C for vein samples and 70 ^{o}C for amygdales, along with $\delta^{18}O$ source fluid calculations suggest a magmatic source fluid for veins (~10‰$_{VSMOW}$) precipitated out of equilibrium with bedrock ambient temperature suggested by the amygdale (~ 1‰) (Section 5.2). Modelling based on vitrinite reflectance data (Marshall et al. 1994) indicates that bond-reordering did not occur and that these temperatures are therefore accurate temperatures of precipitation. When combined with (2), these findings suggest sustained subsurface igneous activity long after surface eruption events ended in the Early- Mid Devonian (Section 5.4).

(4) High fluctuations in minor elements Fe^{2+} (100-5000 ppm) and Mn^{2+} (500-40000 ppm), as well as stable isotopes $\delta^{13}C$ (-1 to -9‰) and $\delta^{18}O$ (-1 to -13‰ $_{VPDB}$) are suggestive of a complex bedrock fluid interaction but are unable to determine evolution in fluid source with growth direction, especially given the limitations present with quantitative analysis using cathodoluminescence imagery in Mn^{2+} rich fluids (Sections 5.3, 5.1 respectively).

(5) LREE enriched, HREE depleted chondrite normalized trends, flat LREE-MREE, depleted HREE bedrock amygdale normalized trends, and largely negative Ce anomalies support a magmatic source fluid, while Eu anomalies suggest a more complex, yet extensive amount of bedrock interaction (Section 5.3).

The methodologies applied within this study show potential for applications to geothermal energy. The use of combined U-Pb LAICPMS calcite dating and clumped isotope paleothermometry overcome previous dating and temperature limitations, and given increased spatial capacity, may be effectively used to assess scaling events within geothermal systems and be applied as one of the analytical tools used to assess the overall economic potential of a geothermal locality.

- REFERENCES -

[SERC] Geochemical Instrumentation and Analysis: Cathudoluminescence Theory. [Internet]. Northfield (MN): Carleton College Science Education Research Centre (SERC); [updated 2016 Nov 10; cited 2018 Jan 14]. Available from: serc.carleton.edu/research_education/ geochemsheets/CLTheory.html.

[USGS] USGS Denver Microbeam Laboratory: The Electron Microprobe. [Internet]. Denver (CO): United States Geological Survey; [updated 2015 Jan 21; cited 2018 Jan 14). Available from: http://usgsprobe.cr.usgs.gov/eprobe1.html

Armstrong H.A., Owen A.W. 2001. Terrane evolution of the paratectonic Caledonides of northern Britain. Joural of the Geological Society 158:475-486.

Armstrong M. & Patterson I.B. 1970. The Lower Old Red Sandstone of the Strathmore Region. Report of the Institute of Geological Sciences, 70/12.

Barker S.L.L., Cox S.F., Eggins S.M., Gagan M.K. 2006. Microchemical evidence for episodic growth of antitaxial veins during fracture-controlled fluid flow. Earth and Planetary Science Letters 250:331-344.

Barker S.L.L., Cox S.F. 2011. Oscillatory zoning and trace element incorporation in hydrothermal minerals: insights from calcite growth experiments. Geofluids 11:48-56.

Bau M., Möller P. 1992. Rare earth element fractionation in metamorphogenic hydrothermal calcite, magnesite, and siderite. Mineralogy and Petrology 45:231-246.

Bergman S.C., Huntington K.W., Crider J.G. 2013. Tracing paleofluid sources using clumped isotope thermometry of diagenetic cements aling the Moab Fault, Utah. American Journal of Science 313: 490-515.

Bluck B.J., Gibbons W., Ingham J.K. 1992. Terranes. Geological Society, London, Memoirs 13:1-4.

Bluck B.J. 2000. Old Red Sandstone basins and alluvial systems of Midland Scotland. In: Friend, P.F. & Williams, B.P.J. (eds) New Perspectives on the Old Red Sandstone. Geological Society, London, Special Publications, 180, 417–437.

Blyth A., Frape S., Ruskeeniemi, T., Blomqvist, R. 2004. Origins, closed system formation and preservation of calcites in glaciated crystalline bedrock: evidence from the Palmottu natural analogue site, Finland. Applied Chemistry 19:675-686.

Bonifacie M., Calmels D., Eiler J.M., Horita J., Caduteau C., Vasconcelos C., Agrinier P., Katz A., Passey B.H., Ferry J.M., Bourrand J.J. 2017. Calibration of the dolomite clumped isotope thermometer from 25 to 350 ^{o}C, and implications for a universal calibration for all (Ca, Mg, Fe)CO_3 carbonates.

all (Ca, Mg, Fe)CO3 carbonates

Bons P.D., Elburg M.A., Gomez-Rivas E. 2012. A review of the formation of tectonic veins and their microstructures. Journal of Structural Geology 43:33-62.

Browne M.A.E., Smith R.A. & Aitken A.M. 2002. Stratigraphical framework for the Devonian (Old Red Sandstone) rocks of Scotland south of a line from Fort William to Aberdeen. British Geological Survey Research Report.

Coggon R.M., Teagle D.A.H. 2011. Hydrothermal calcium-carbonate veins reveal past ocean chemistry. TrAC Trends in Analytical Chemistry (30) 8:1252-1268.

Coogan L.A., Parrish R.R., Roberts N.M.W. 2016. Early hydrothermal carbon uptake by the oceanic crust: Insight from in situ U-Pb dating. Geology 44:147-150.

Dallmeyer R.D., Strachan R.A., Rogers G., Watt G.R. Friend C.R.L. 2001. Dating deformation and cooling in the Scandian thrust nappes of north Sutherland, Scotland: Insights from 40Ar/39Ar and Rb- Sr chronology. Journal of the Geological Society, London 158 (3): 501–512.

Dennis K.J., Affel H.P., Passey B.J., Schrag D.P., Eiler J.M. 2011. Defining and absolute reference frame for 'clumped' isotope studies of CO_2. Geochimica et Cosmochimica Acta 75:7117-7131.

Denniston R.F., Shearer C.K., Layne G.D., Vaniman D.T. 1997. SIMS analyses of minor and trace element distributions in fracture calcite from Yucca Mountain, Nevada, USA. Geochimica et Cosmochimica Acta (61) 9:1803-1818.

DESA (Department of Social and Economic Affairs), United Nations, 2017. World Population Prospects: the 2017 Revision [Internet]. [Cited January 5, 2018]. Available from: https://www.un.org/development/desa/publications/world-population-prospects-the-2017-revision.html

DiPippo R. 2008. Geothermal Power Plants, 2nd ed: Principles, Applications, Case Studies and Environmental Impact. Butterworth-Heinemann 490 p.

Eiler J.M. 2007. “Clumped-isotope” geochemistry—The study of naturally-occurring, multiply-substituted isotopologues. Earth and Planetary Science Letters 262:309–327.

Eiler J.M. 2011. Paleoclimate reconstruction using carbonate clumped isotope thermometry. Quaternary Science Reviews 30:3575-3588.

George T.N. 1960. The stratigraphical evolution of the Midland Valley. Trans. geol. Soc. Glasgow, 24, 32-107

Geothermal Energy Association (GEA). 2013. Geothermal: International Market Overview Report.

Glassley W.C. 2015. Geothermal Energy: Renewable Energy and the Environment, 2nd edition. Boco Raton (FL): CRC Press 490 p.

Guo W., Mosenfelder J.L., Goddard III W.A., Eiler J.M. 2009. Isotopic fractionation associated with phosphoric acid digestion of carbonate minerals: Insights from first principles theoretical modeling and clumped isotope measurements. Geochimica et Cosmochimica Acta 73:7203-7225.

Henkes G.A., Passey B.H., Grossman E.L., Shenton B.J., Pérez-Huerta A., Yancey T.E. 2014. Temperature limits for the preservation of primary calcite clumped isotope paleothermometers. Geochimica et Cosmochimica Acta 139:362-382.

Hilgers C., Koehn D., Bons P.D., Urai J.L. 2000. Development of crystal morphology during unitaxial growth in a progressively widening vein: II. Numerical simulations of the evolution of antitaxial fibrous veins. Journal of Structural Geology 23:873–885.

Hilgers C., Dilg-Gruschinski K., Urai J.L. 2004. Microstructural evolution of syntaxial veins formed by advective flow. Geology 33:261-264.

Hilgers C., Sindern S. 2005. Textural and isotopic evidence on the fluid source and transport mechanism of antitaxial fibrous microstructures from the Alps and the Appalachians. Geofluids 5:239-250.

Hole M., Jolley D., Hartley A., Leleu S., John N., Ball M. 2013. Lava–sediment interactions in an Old Red Sandstone basin, NE Scotland. Journal of the Geological Society, London 170:641–655.

Jochum K.P., Scholz D., Stoll B., Weis U., Wilson S.A., Yang Q., Schwalb A., Börner N., Jacob D.E., Andreae M.O. 2012. Accurate trace element analysis of speleotherms and biogenic calcium carbonates by LA-ICP-MS. Chemical Geology 318-319:31-44.

Kelson J.R., Huntington K.W., Schauer A.J., Saenger C., Lechler A.R. 2017. Toward a universal carbonate clumped isotope calibration: Diverse synthesis and preparatory methods suggest a single temperature relationship. Geochimica et Cosmochimica Acta 197:104-131.

Kennedy W.Q. 1958. The Tectonic Evolution of the Midland Valley of Scotland. Transactions of the Geological Society of Glasgow 23:106-133.

Kim S.T., O'Neil J.R. 1997. Equilibrium and nonequilibrium oxygen isotope effects in synthetic carbonates. Geochimica et Cosmochimica Acta 61:3461-3475.

Lee Y.J., Wilitschko D.V., Grossman E.L., Morse J.W., Lamb W.M. 1997. Sequential vein growth with fault displacement: An example from the Austin Chalk Formation, Texas. Journal of Geophysical Research 102:22611-22628.

LeRouge C., Claret F., Denecke M.A., Wille G., Falkenberg G., Ramboz C., Bény C., Giffaut E., Schäfer T., Gaucher E.C. 2010. Comparative EPMA and -XRF methods for mapping micro-scale distribution of iodine in biocarbonates of the Callovian-Oxfordian clayey formation at Bure, Eastern part of the Paris Basin. 12th International Conference on the Chemistry and Migration Behaviour of Actinides and Fission Products in the Geosphere (Migration '09). Kennewick, WA. 18 pp.

Lloyd M.K., Eiler J.M., Nabelek P.I. 2017. Clumped isotope thermometry of calcite and dolomite in a contact metamorphic environment. Geochimica et Cosmochimica Acta 197:323-344.

MacDonald J.M., John C.M., Girard J.P. 2017. Testing clumped isotopes as a reservoir characterization tool: a comparison with fluid inclusions in a dolomitized sedimentary carbonate reservoir buried to 2-4km. In: From Source to Seep: Geochemical Applications in Hydrocarbon Systems. Geological Society, London, Special Publications 468:189-202.

Machel H.G. 1985. Cathudoluminescence in calcite and dolomite and its chemical interpretation. Geoscience Canada 12:139-147.

Marshall J.E.A., Haughton P.D.W., Hillier S.J. 1994. Vitrinite reflectivity and the structure and burial history of the Old Red Sandstone of the Midland Valley of Scotland. Journal of the Geological Society, London 151:425-438.

Maskenskaya O.M., Drake H., Åström M.E. 2013. Geochemistry of calcite veins: records of fluid mixing and fluid-rock interaction. Procedia Earth and Planetary Science 7:566–569.

Maskenskaya O.M., Drake H., Broman C., Hoghalm J.K., Czuppon G., Åström M.E. 2015. Source and character of syntaxial hydrothermal calcite veins in Paleoproterozoic crystalline rocks revealed by fine-scale investigations. Geofluids 14:495-511.

McDonough W.F., Sun S.S. 1995. The composition of the Earth. Chemical Geology 120 (3-4):223-253.

McNamara D.D., Lister A., Prior D.J. 2016. Calcite sealing in a fractured geothermal reservoir: Insights from combined EBSD and chemistry mapping. Journal of Volcanology and Geothermal Research 323:38-52

Mendrum J.R. 2012. Late Caledonian (Scandian) and Proto-Variscan (Acadian) orogenic events in Scotland. [Internet]. British Geological Survey, Edinburgh. [cited March 27 2018] Available from: nora.nerc.ac.uk.

Möller P., Lüders V., Schröder J., Luck J. 1991. Element partitioning in calcite as a function of solution flow rate: a study on vein calcites from the Harz Mountains. Mineralium Deposita 26:175-179.

Morad S., Al-Aasm I.S., Sirat M., Sattar M.M. 2010. Vein calcite in cretaceous carbonate reservoirs of Abu Dhabi: Record of origin of fluids and diagenetic conditions. Journal of Geochemical Exploration 106:156-170.

Parry S.F., Noble S.R., Crowley Q.G., Wellman C.H. 2011. A high-precision U–Pb age constraint on the Rhynie Chert Konservat-Lagerstätte: time scale and other implications. Journal of the Geological Society, London 168:863–872.

Ramsay J.G. 1980. The crack-seal mechanism of rock deformation. Nature 284:135-139.

Rawley H.J. 2015. Lava-water-sediment interaction: processes, products and petroleum systems [dissertation]. University of Glasgow. 275 p.

Robert M. MacKay Electron Microprobe Lab [Internet]. Halifax (NS): Dalhousie University; [cited 2018 Jan 14]. Available from: www.dal.ca/sites/electron-microprobe-lab.html

Roberts N.M.W., Rasbury T., Parrish R.R., Smith C.J., Horstwood M.S.A., Condon D.J. 2016. A calcite reference material for LA-ICP-MS U-Pb geochronology. AGU Geochemistry, Geophysics, Geosystems 2804-2817.

Roberts N.M.W., Walker R.J. 2016. U-Pb geochronology of calcite-mineralized faults: Absolute timing of rift-related fault events on the northeast Atlantic margin. Geology 44:531-534.

Rollinson H.R. 1993. Using Geochemical Data: Evaluation, Presentation, Interpretation. Pearson Education Limited 380 p.

Ryb B, Lloyd M.K., Stolper D.A., Eiler J.M. 2017. The clumped-isotope geochemistry of exhumed marbled from Naxos, Greece. Earth and Planetary Science Letters 470:1-12.

Sandström B., Tullborg E.L. 2009. Episodic fluid migration in the Fennoscandian Shield recorded by stable isotopes, rare earth elements and fluid inclusions in fracture minerals at Forsmark, Sweden. Chemical Geology 266 (3):126-142.

Schauble E.A., Ghosh P., Eiler J.M. 2006. Preferential formation of ^{13}C-^{18}O bonds in carbonate minerals, estimated using first principles lattice dynamics. Geochimica Cosmochimica Acta 7:2510-2529.

Simmons S.F., Christenson B.W. 1993. Towards a unified theory on calcite formation in boiling geothermal systems. Proceedings 15th Geothermal Workshop; NZ.

Stone P. 2014. A review of geological origins and relationships in the Ballantrae Complex, SW Scotland. Published online: http://nora.nerc.ac.uk/507349/ British Geological Survey, 60p.

Sturrock C.P., Catlos E.J., Miller N.R., Akgun A., Fall A., Gabitov R.I., Yilmaz I.O., Larson T., Black K.N. 2017. Fluids along the North Anatolian Fault, Niksar basin, north central Turkey: Insight from stable isotopic and geochemical analysis of calcite veins. Journal of Structural Geology 101:58-79.

Sumner K.K., Camp E.R. Huntington K.W., Cladouhos T.T., Uddenberg M. 2015. Assessing fracture connectivity using stable and clumped isotope geochemistry of

calcite cements. PROCEEDINGS, Fortieth Workshop on Geothermal Reservoir Engineering. 12 pp.

Thirlwall M.F. 1981. Implications for Caledonian plate tectonic models of chemical data from volcanic rocks of the British Old Red Sandstone. Journal of the Geological Society, London 138:123–138.

Thirlwall M.F. 1982. Systematic variation in chemistry and Nd–Sr isotopes across a Caledonian calc-alkaline volcanic arc: Implications for source materials. Earth and Planetary Science Letters 58:24–50

Thirlwall M.F. 1983. Isotope geochemistry and origin of calc-alkaline lavas from a Caledonian continental margin volcanic arc. Journal of Volcanology and Geothermal Research 18:589–631.

Thirlwall M.F. 1988. Geochronology of Late Caledonian magmatism in northern Britain. Journal of the Geological Society, London 145:951–967.

Trewin N.H. & Thirlwall M.F. 2002. Old Red Sandstone. In: Trewin NH. (ed.) The Geology of Scotland, 4th edn. Geological Society, London 213–249.

Tulloch A.J., 1982. Mineralogical Observations on Carbonate Scaling in Geothermal Wells at Kawerau and Broadlands. Proceedings 4th New Zealand Geothermal Workshop.

Uysal I.T., Zhao J.X., Golding S.D., Lawrence M.G., Glikson M., Collerson K.D. 2007. Sm–Nd dating and rare-earth element tracing of calcite: Implications for fluid-flow events in the Bowen Basin, Australia. Chemical Geology 238:63-71.

Veizer J., Ala D., Azmy K., Bruckschen P., Buhl D., Bruhn F., Carden G.A.F., Diener A., Stefan E., Godderis Y., Jasper T., Korte C., Pawallek F., Podlaha O.G., Strauss H. 1999. $^{87}Sr/^{86}Sr$, d 13C and $\delta^{18}O$ evolution of Phanerozoic seawater. Chemical Geology 161:59-88.

Wogelius R.A., Fraser D.G., Wall G.R.T., Grime G.W. Trace element and isotopic zonation in vein calcite from the Mendip Hills, UK, with spatial-process correlation analysis. Geochimica et Cosmochimica Acta (61) 10:2037-2051.

Woodcock N., Strachan R. 2008. Geological history of Britain and Ireland, Wiley-Blackwell.

- APPENDICES -

Appendix 1: Raw data and calibrations included in this study for EMPA, Stable Isotope, Clumped Isotope, U-Pb LA ICPMS, and Trace Element LA-ICPMS analyses. See attached Microsoft Excel spreadsheet.